CANCER

TP53 missense–specific transcriptional plasticity drives resistance against cell cycle inhibitors in pancreatic cancer

Laura Urbach[1,2], Lena Wieland[1,3], Frederike Penz[1], Rebecca Diya Samuel[1], Stefan Küffer[4], Lukas Klein[1], Christof Lenz[5,6], Ulrich Sax[7,2], Michael Ghadimi[3,2], Ramona Schulz-Heddergott[8,2], Elisabeth Hessmann[1,2], Volker Ellenrieder[1,2], Nelson Dusetti[9], Shiv K. Singh[1,2]*

In ~70% of patients with pancreatic ductal adenocarcinoma, the *TP53* gene acquires gain-of-function (GOF) mutations leading to rapid disease progression. Specifically, missense p53 (misp53) GOF mutations associate with therapy resistance and worse clinical outcomes. However, the molecular functions of distinct misp53 mutants in plasticity and therapy response remain unclear. Integrating multicenter patient data and multi-omics, we report that the misp53$^{R273H/C}$ mutant is associated with cell cycle progression and a basal-like state compared to the misp53$^{R248W/Q}$ mutant. Loss of misp53$^{R273H/C}$ decreased tumor growth and liver metastasis while prolonging survival in preclinical models. We found that misp53$^{R273H/C}$ specifically regulated the Rb/DREAM axis involved in cell cycle regulation. Notably, a clinical CDK4/6 inhibitor reduced misp53$^{R273H/C}$ mutant expression. However, it triggered MAPK/ERK-mediated resistance mechanisms, enhancing cell survival and resistance to CDK4/6 inhibitors. Combining MAPK/ERK and CDK4/6 inhibitors reduced misp53$^{R273H/C}$-associated oncogenic functions. Thus, distinct misp53 mutants show unique cell-intrinsic plasticity, therapeutic vulnerabilities, and resistance mechanisms.

INTRODUCTION

Pancreatic ductal adenocarcinoma (PDAC) ranks among the most aggressive cancers with a 5-year survival rate of only 11% (*1*). Currently, the only curative treatment option is surgery followed by adjuvant chemotherapy, which is applicable for 15 to 20% of patients with PDAC (*2*–*4*). Most cases present locally advanced or metastatic disease treated with gemcitabine/nab-paclitaxel or modified FOLFIRINOX (mFOLFIRINOX) (*5*). However, resistance to therapy and frequent tumor recurrence limit the success rates of conventional therapeutic regimens (*6*). PDAC is characterized by a complex interplay of genetic, transcriptional, and environmental factors, which substantially contribute to tumor heterogeneity promoting disease complexity, thus, presenting a formidable challenge to available therapy options (*7*). This highlights the need to refine the molecular understanding of PDAC heterogeneity and stratification-based therapeutic interventions to prolong patient outcomes.

Tumor suppressor inactivation and missense mutations in PDAC are strongly linked to increased cell cycle, metastatic progression and therapeutic resistance (*8*). More than 90% of patients with PDAC show activating *KRAS* mutations, while more than 70% of cases exhibit alterations in the *TP53* gene, which are associated with G_1-S cell cycle dysregulation (*8*, *9*). *TP53* mutations are highly prevalent in patients with poorly differentiated “basal-like” (BL) and advanced stage cases (*9*, *10*). The BL subtype is associated with a worse prognosis and poor response to gemcitabine-based or mFOLFIRINOX therapy compared to the “classical” (CLA) subtype (*11*–*13*). *TP53* missense mutations and cell cycle regulatory pathways, such as “E2F targets” and “G_2-M checkpoint, “are linked to BL state and disease aggressiveness in these PDAC transcriptional subtypes (*10*, *12*, *14*). However, it remains unclear how distinct p53 mutants contribute to PDAC plasticity and disease aggressiveness.

Specific missense mutations in the *TP53* gene (misp53) can lead to formation of distinct structural or conformational mutant p53 variants that lose tumor suppressive properties (loss of function, LOF) and, additionally, acquire new oncogenic functions (gain of function, GOF) (*15*, *16*). A recent study has shown that the presence of GOF misp53 mutants is substantially associated with poor clinical outcomes in patients with PDAC compared to non-GOF misp53 variants. This is likely due to high tumor recurrence and a locally advanced pathological state associated with GOF misp53 (*17*). Given the heterogeneity of *TP53* mutations in cancer, there is an increasing interest in interrogating mutation-specific GOFs that can be of potential therapeutic relevance (*18*–*20*). In the case of PDAC, different misp53 mutants associate with specific interaction partners, thereby influencing transcriptional and functional activities that promote tumor progression (*21*, *22*). The three key misp53 mutants in PDAC arise from hotspot missense mutations at codons R175 (~5.3%), R248 (~5.3%), and R273 (~5.8%), together accounting for almost 17% of all *TP53*-mutated PDAC cases (*23*); they are among the GOF misp53 mutants in patients with PDAC. The misp53^{R175H} mutant (misp53^{R175H}) has been linked to KRAS^{G12D}-induced tumor initiation through its mouse homolog misp53^{R172H} within the widely used genetically engineered mouse model KPC (*LSL-Kras*$^{G12D/+}$; *LSL-Trp53*$^{R172H/+}$; *Pdx-1-Cre*) (*24*). Further, several studies have associated GOF misp53^{R175H} to PDAC progression

---

[1]Department of Gastroenterology, Gastrointestinal Oncology and Endocrinology, University Medical Center Göttingen, Göttingen, Germany. [2]Clinical Research Unit 5002 (CRU5002/KFO5002), University Medical Center Göttingen, Göttingen, Germany. [3]Department of General, Visceral, and Pediatric Surgery, University Medical Center Göttingen, Göttingen, Germany. [4]Institute of Pathology, University Medical Center Göttingen, Göttingen, Germany. [5]Core Facility Proteomics, University Medical Center Göttingen, Göttingen, Germany. [6]Bioanalytical Mass Spectrometry Group, Max Planck Institute for Multidisciplinary Sciences, Göttingen, Germany. [7]Department of Medical Informatics, University Medical Center Göttingen, Göttingen, Germany. [8]Department of Molecular Oncology, University Medical Center Göttingen, Göttingen, Germany. [9]Centre de Recherche en Cancérologie de Marseille, CRCM, Inserm, CNRS, Institut Paoli-Calmettes, Université Aix-Marseille, Marseille, France.
*Corresponding author. Email: shiv.singh@med.uni-goettingen.de

(*21*, *25*–*27*). However, the molecular and pathological functions of the misp53$^{R248Q/W/L}$ and misp53$^{R273H/C}$ mutants in PDAC aggressiveness and subtype plasticity remain largely unclear.

Our study focused on the misp53$^{R273H/C}$ and misp53$^{R248Q/W/L}$ hotspot mutations in PDAC plasticity and their importance in patient stratification and potential therapeutic interventions. We carried out genomic, transcriptional, and proteomic analyses using established and patient-derived xenograft (PDX) cell lines, human patients' tissue samples, and preclinical mouse models to unravel the molecular functions of the DNA contact mutant misp53$^{R273H/C}$ and its MAPK/ERK compensatory mechanism in cell cycle plasticity, subtype specificity, and disease aggressiveness. Our findings suggest that combined targeting of CDK4/6-mediated cell cycle progression by palbociclib and the mitogen-activated protein kinase/extracellular signal–regulated kinase (MAPK/ERK) pathway by trametinib can overcome misp53$^{R273H/C}$-associated cellular plasticity in PDAC. Our study offers a comprehensive understanding of how hotspot missense mutations in the *TP53* gene contribute to transcriptional plasticity and therapeutic vulnerabilities in PDAC, which can help improve patient stratification and treatment outcomes.

RESULTS

Misp53 mutations relate to diverse cell type–specific transcriptional programs

The combination of TCGA (*28*), ICGC (*29*), and QCMG (*9*) PDAC patient cohorts, based on the *TP53* gene mutational status, showed dominance of missense mutations that predominantly occurred within the DNA binding domain of the gene. These mutations, which were most frequent at the codons 175, 248 and 273, render the tumor suppressor protein p53 dysfunctional (LOF) (Fig. 1A). This is due to an exchange of the native arginine amino acid mostly with histidine, cysteine, tryptophan, or glutamine, resulting in either DNA contact (248 and 273) or structural (175) mutants leading to a loss of DNA binding ability or a misfolded protein, respectively (*30*–*32*). These mutations can acquire new oncogenic GOFs, potentially supporting tumor progression (*15*, *16*). Our University Medical Center (UMG)–associated patient cohorts also revealed misp53 hotspots at codons 248 and 273, highlighting the importance of the DNA contact mutants misp53$^{R273H/C}$ and misp53$^{R284Q/W/L}$ (Fig. 1B). To investigate the molecular plasticity of distinct misp53 mutants on lineage transcriptional changes and subtype specificity, established PDAC cell lines carrying the misp53^{R273H} or misp53^{R248W} hotspot mutations, respectively, were used for transient small interfering RNA (siRNA)–mediated knockdown (Fig. 1, C and D). Transcriptional changes were analyzed by condition comparison in RNA sequencing (RNA-seq) (fig. S1, A to D). Gene Set Enrichment Analysis (GSEA) revealed that knockdown of the misp53^{R248W} variant mainly associated with a range of pathways such as MYC signaling, epithelial-to-mesenchymal transition (EMT) or oxidative phosphorylation, indicating diverse functions (Fig. 1E). In contrast, silencing of misp53^{R273H} induced, but also down-regulated, distinctive signatures associated with PDAC subtype and disease aggressiveness. Among the top significantly altered key hallmark gene sets that positively associated with misp53^{R273H} expression were the cell cycle signatures E2F targets, G_2-M checkpoint, and "mitotic spindle" (Fig. 1F). Cell cycle–associated E2F, G_2-M checkpoint, and EMT gene signatures have previously been linked to BL PDAC subtype identity, advanced stage disease, and therapy resistant phenotype (*8*, *12*, *33*). Further validation of our RNA-seq analysis revealed that most of the down-regulated gene sets upon misp53^{R273H} depletion were of the aggressive BL subtype (e.g., MYC, TNF-α, and KRAS signaling) of PDAC (Fig. 1F and fig. S1E) (*12*, *33*), while the induced pathways (e.g., "cholesterol homeostasis") positively correlated with the CLA PDAC subtype (Fig. 1F and fig. S1E) (*12*). Analysis of curated (C2) gene sets linked to cell cycle progression and PDAC aggressiveness confirmed a strong positive correlation between misp53^{R273H} and cell cycle–associated transcriptome signatures (e.g., G_1- and S-phase, cyclin A, and CDK2) and BL subtype- specificity (Fig. 1, G and H). Transient and genetic knockdown of misp53^{R273H} up-regulated CLA-specific markers, such as GATA6 and ECAD, and down-regulated the EMT marker vimentin ("VIM") (fig. S1, F to H). These findings strongly suggested that the misp53^{R273H} mutant was particularly linked to cell cycle programs and plasticity compared to misp53^{R248W} in PDAC aggressiveness.

The misp53$^{R273H/C}$ mutant binds to E2F motifs and associates with cell cycle programs

To further determine the involvement of misp53^{R273H} in cell cycle progression and plasticity, we performed misp53^{R273H} and misp53^{R248W} chromatin immunoprecipitation sequencing (ChIP-seq) experiments. Previous studies have suggested that DNA contact misp53 mutants can sequester intact transcription factors (TFs) to reinstate DNA binding capability and facilitate transcriptional regulation (*19*, *21*, *22*). We found that both misp53^{R273H} and misp53^{R248W} bound to various sites in the genome, including promoters, exons, enhancers, and untranslated regions (Fig. 2, A and B). However, misp53^{R273H} showed stronger binding to promoters and transcription start sites (TSS) compared to misp53^{R248W} (Fig. 2C). We also examined the TF motifs at misp53-specific genomic binding sites to predict potentially regulated pathways (Fig. 2D and table S1). We found that E2F family motifs were more prevalent at misp53^{R273H}-specific binding sites than at those associated with misp53^{R248W} (Fig. 2D). E2F proteins are known to control cell cycle with some activating cell cycle transcription (e.g., E2F1) and others repressing it (e.g., E2F4) (*34*). Our findings suggested that misp53^{R273H} might influence cell cycle progression by regulating E2F-related target genes. To validate this hypothesis, we analyzed transcriptome data from TCGA (*28*) and QCMG (*9*) patient cohorts and found that patients with PDAC and *TP53* mutations had elevated scores for cell cycle gene sets compared to patients with wild-type (WT) *TP53* (Fig. 2, E to J). This observation is consistent with a previous study on patients with PDAC (*8*). Notably, patients with misp53$^{R273H/C}$ mutations showed relatively higher scores, indicating increased cell cycle activity and progression (Fig. 2, E to J). We also observed similar trends for E2F1 and G_1-S phase–related signatures (fig. S2, A and B). In addition, we found that the BL gene set "Hallmark EMT" exhibited relatively higher scores in patients with mutated p53, specifically in those with the misp53$^{R273H/C}$ mutation, while the CLA signature 'Hallmark KRAS Signaling Down' showed lower scores (fig. S2, C and D). Overall, our results suggest that misp53$^{R273H/C}$ is involved in cell cycle regulation and progression, contributing to the PDAC plasticity.

Loss of misp53$^{R273H/C}$ impairs cell cycle progression and inhibits tumor growth

To investigate the effect of misp53$^{R273H/C}$ on cell cycle progression, we silenced misp53$^{R273H/C}$ or misp53$^{R248W/Q}$ and carried out flow

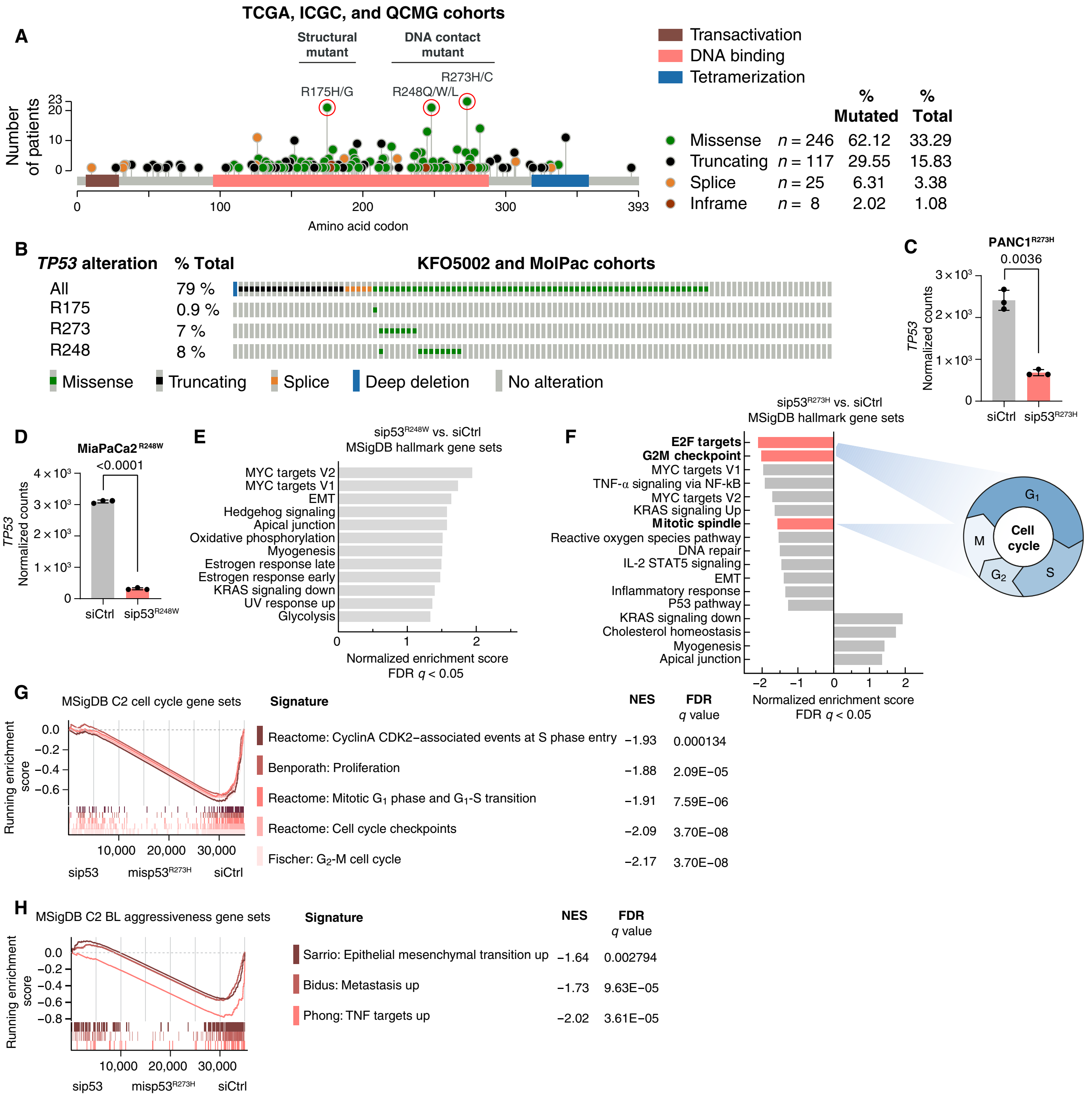

Fig. 1. *TP53* hotspot missense mutations are associated with distinct transcriptional programs. (**A**) cBioPortal (*23*) mutational profile of the *TP53* gene locus in the TCGA (*28*), ICGC (*29*), and QCMG (*9*) PDAC patient cohorts (total patients, *n* = 739; *TP53*-mutated patients, *n* = 396). Red circles indicate hotspot *TP53* missense mutations (misp53). (**B**) Hotspot misp53 analysis of the KFO5002 and MolPac internal PDAC cohorts of the UMG Göttingen (UMG) (total patients, *n* = 76). (**C** and **D**) Knockdown of *TP53* transcript from the misp53^{R273H} silencing (sip53^{R273H}, red) versus control siRNA (siCtrl, gray) RNA-seq in PANC1 (C) and the misp53^{R248W} silencing (sip53^{R248W}, red) versus control siRNA (siCtrl, gray) RNA-seq in MiaPaCa2 (D). Normalized counts with means ± SD shown. *n* = 3 per condition. (**E** and **F**) GSEA analysis for MSigDB Hallmark gene sets with *q* value <0.05 in the differentially expressed genes of the sip53^{R248W} versus siCtrl RNA-seq in MiaPaCa2 (E) and the sip53^{R273H} versus siCtrl RNA-seq in PANC1 (F). Highlighted gene sets are associated to the cell cycle (F). *n* = 3 per condition. (**G** and **H**) GSEA plots for cell cycle–related MSigDB curated (C2) gene sets (G) and BL aggressiveness–related MSigDB curated (C2) gene sets (H) of the sip53^{R273H} versus siCtrl RNA-seq in PANC1. Normalized enrichment score (NES) and false discovery rate (FDR) *q*-value are indicated.

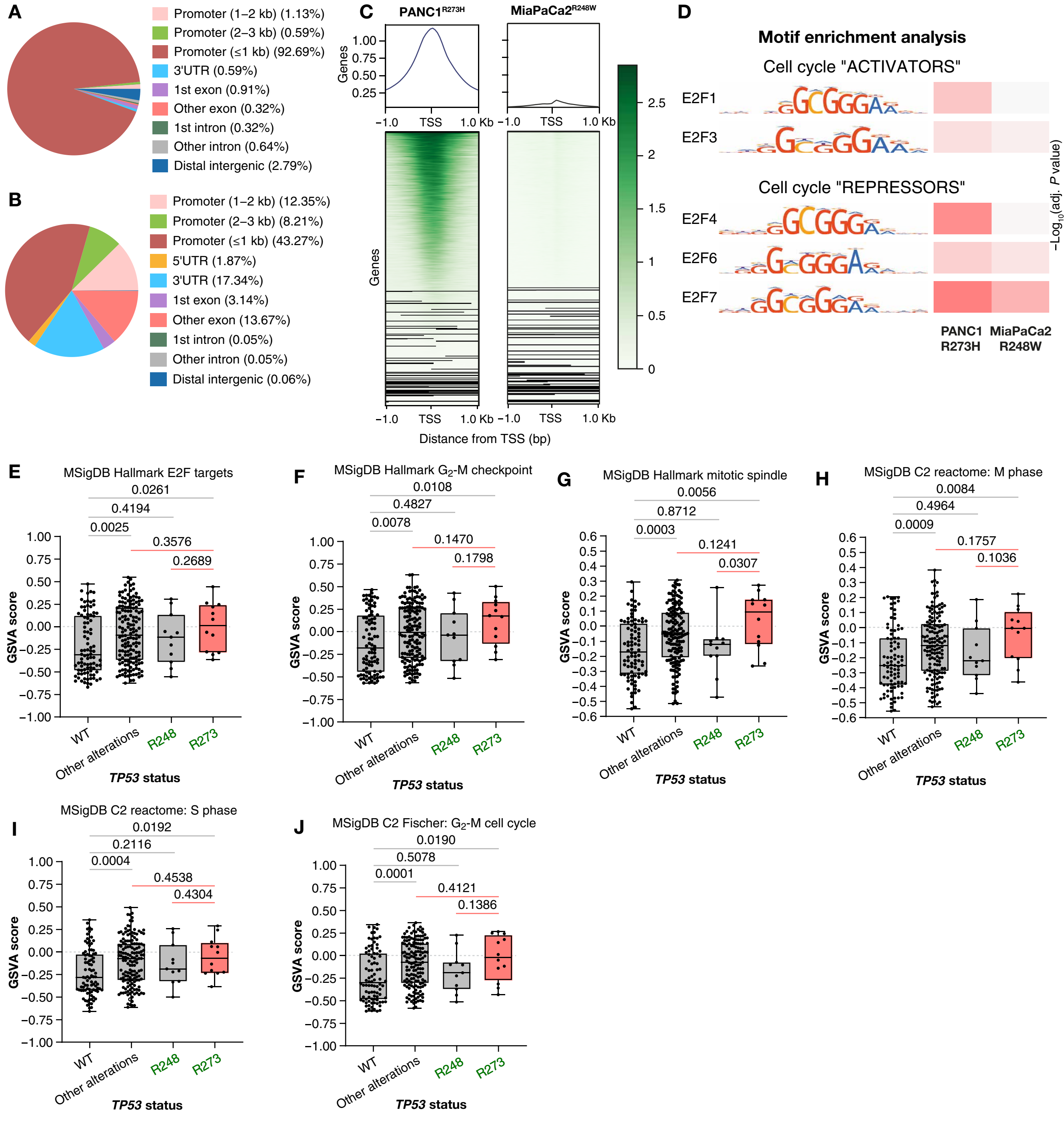

Fig. 2. The genome-wide binding of misp53^{R273H} is associated with E2F cell cycle signatures. (**A** to **D**) Genomic annotation of misp53^{R273H}-specific (A) and misp53^{R248W}-specific (B) binding sites, determined by peak overlap of misp53^{R273H} and misp53^{R248W} ChIP-seqs in PANC1 and MiaPaCa2, respectively. The coverage of misp53^{R273H}- and misp53^{R248W}-specific ChIP-seq peaks over TSS is shown in (C). The motif enrichment analysis of misp53^{R273H}- and misp53^{R248W}-specific ChIP-seq peaks is shown in (D) with motif sequences displayed and $-\log_{10}$(adjusted P values) indicated as a heatmap. $n = 1$. (**E** to **J**) GSVA scores of publicly available RNA-seq data from 265 patients of the TCGA (*28*) and QCMG (*9*) PDAC patient cohorts for MSigDB Hallmark gene sets E2F targets (E), G$_2$-M checkpoint (F), and mitotic spindle (G), and curated (C2) gene sets "Reactome: M phase" (H), "Reactome: S phase" (I), and "Fischer: G$_2$-M cell cycle" (J). Patients were stratified according to their *TP53* mutational status: wildtype "WT," all mutations/deletions except codons R248 and R273 "other alterations," hotspot missense mutations at codon R248 "R248" and R273 "R273." Values are displayed in boxplots indicating median, quartiles, and min/max values, and each dot represents the GSVA score of one patient. The *P* values are indicated and determined by Student's t-test with Welch's correction.

cytometry analysis using established and PDX cell lines (Fig. 3, A to E, and fig. S3, A to E). Silencing of misp53$^{R273H/C}$ caused a G_1 arrest in all misp53$^{R273H/C}$-specific PDAC models (Fig. 3, A to C, and fig. S3, A to C), while silencing of misp53$^{R248W/Q}$ had no effect on the cell cycle arrest (MiaPaCa2^{R248W}; Fig. 3D and fig. S3D); it rather reduced the number of cells in G_1 phase in PDAC021T^{R248Q} cells (Fig. 3E and fig. S3E). To understand these misp53$^{R273H/C}$-specific cell cycle inhibitory effects, the expression of different G_1-S phase proteins was analyzed upon misp53$^{R273H/C}$ or misp53$^{R248W/Q}$ silencing. Cyclin A and cyclin E levels were explicitly reduced upon misp53^{R273H} loss compared to misp53^{R248W} silencing (Fig. 3F), which greatly aligned with the transcriptome data upon misp53^{R273H} ablation (Fig. 1, F and G). However, the protein expression of cyclin D2, cyclin D3, CDK6, and CDK2 remained unchanged (Fig. 3F). Validation of cyclin A and cyclin E reduction using two different p53 siRNA sequences and misp53$^{R273H/C}$- and misp53$^{R248W/Q}$-specific PDX cell lines again implied misp53$^{R273H/C}$ specificity (Fig. 3, G to I, and fig. S3F). In addition, transient overexpression of misp53^{R273H} in L3.6 p53^{null} cells could effectively induce cyclin A and cyclin E expression (fig. S3, G and H). These findings strongly suggest that the misp53$^{R273H/C}$ mutant positively regulates cell cycle progression through the G_1-S phase machinery in PDAC.

To assess the differences in the proliferation rates between the misp53^{R273} and misp53^{R248} tumors, we examined the tumor growth rates of PDX specimens (Fig. 3, J to M). This assessment involved a series of subcutaneous tumor implantations of primary PDAC patient specimens harboring the misp53$^{R273H/C}$ or misp53$^{R248W/Q}$ mutants in PDX murine models (Fig. 3J). The comparison revealed that tumors with the misp53$^{R273H/C}$ mutations reached a diameter of 1 cm significantly faster than those with the misp53$^{R248W/Q}$ mutations (Fig. 3K). In addition, elevated levels of the proliferation marker Ki67 confirmed that the misp53$^{R273H/C}$-specific tumors exhibited a higher rate of proliferation and growth (Fig. 3, L and M). Next, we examined survival and disease aggressiveness, including metastasis, related to the misp53^{R273H} and misp53^{R248W} mutants using pancreas-specific orthotopic mouse models. These models were created by transplanting stable knockdown cell lines of misp53^{R273H} and misp53^{R248W} into the pancreas of immunocompromised mice (Fig. 3N and fig. S3, I to L). Our findings indicated that the misp53^{R273H} knockdown group (sh*TP53*^{R273H}) displayed improved survival, reduced tumor weight, and fewer visible liver metastases compared to control mice [empty vector (EV)] (Fig. 3, O to Q). In contrast, the misp53^{R248W} knockdown group (sh*TP53*^{R248W}) did not show differences in median survival or tumor weight compared to controls (EV) (fig. S3, M to O). In summary, these results demonstrate that the misp53$^{R273H/C}$ mutations specifically affect G_1-S cell cycle progression by regulating the expression of crucial oscillating factors that drive PDAC proliferation, growth, and progression to metastatic disease.

Misp53$^{R273H/C}$ interacts with the cell cycle repression machinery to indirectly promote cell cycle progression

To gain insights into the mechanism of misp53-mediated control over the cell cycle machinery, we focused on misp53^{R273H} and its interaction with cell cycle activator and repressor TFs that regulate cell cycle progression. Our findings of the misp53^{R273H} transcriptome (Fig. 1) as well as ChIP-seq analysis (Fig. 2, A to D) revealed a notable association with the E2F family activator and repressor TFs (Fig. 2D), which play a crucial role in controlling cell cycle progression (*34*). Therefore, we investigated how misp53$^{R273H/C}$ affects E2F proteins and cell cycle regulation. Although silencing of misp53^{R273H} did not alter E2F1 (i.e., cell cycle activator TF) levels in PDAC cells (Fig. 4A), previous studies suggested that misp53 mutants could form protein-protein complexes to execute their GOFs (*21*, *22*, *35*). However, our co-immunoprecipitation (Co-IP) experiments did not detect any physical interaction between misp53^{R273H} and E2F1 (Fig. 4B). Therefore, we extended this analysis by performing an unbiased mass spectrometry experiment in both misp53^{R273H} and misp53^{R248W}-specific PDAC cell line. This revealed multiple proteins linked to chromatin regulators [e.g., Retinoblastoma-binding protein 4 (RBBP4) and histone deacetylases (HDACs)] that interacted with both misp53^{R273H} and misp53^{R248W} mutants (Fig. 4C and fig. S4A). Notably, EIF6 and distinct histone proteins, specifically H1-5, demonstrated unique interactions with misp53^{R273H} compared to misp53^{R248W}. In particular, these histone proteins could interact with RBBP4 chromatin remodeling complexes to regulate gene expression (Fig. 4C) (*36*). RBBP4 is crucial for cell cycle regulation and acts as a key component of the transcription machinery involved in controlling the cell cycle, especially within the dimerization partner, RB-like, E2F and multi-vulval class B (DREAM) complex (*37*). It can interact with the retinoblastoma protein (Rb) to regulate the expression of genes related to the cell cycle, and Rb has been implicated in controlling the G_1-S transition and PDAC aggressiveness (*38*–*41*). Given these findings, we investigated the potential interactions with Rb pathways to understand how misp53 mutants regulate cell cycle repression in PDAC. Targeted Co-IP experiments showed a strong interaction between misp53^{R273H} and p-Rb, the hyperphosphorylated (inactive) form of Rb (Fig. 4D). In contrast, misp53^{R248W} did not interact with either p-Rb or Rb proteins (fig. S4B). These findings imply that misp53^{R273H} mutants may sequester active Rb from inhibiting the cell cycle, thereby promoting progression. In line with these key findings, the depletion of misp53$^{R273H/C}$ across three different established and PDX cell lines resulted in decreased p-Rb phosphorylation (Fig. 4, E to G). This suggested a transition from inactive Rb to active Rb, crucial for cell cycle inhibition. We therefore hypothesized that Rb activation might repress E2F promoters and halt cell cycle progression upon the loss of misp53$^{R273H/C}$ (Fig. 4H). Our Rb ChIP analyses showed increased binding of active Rb to the E2F1 promoter after the silencing of misp53$^{R273H/C}$ in both established and PDX cell lines, suggesting suppression of E2F-mediated transcription (Fig. 4I and fig. S4, C to E). However, when we assessed Rb binding to other known Rb target promoters, we did not observe a considerable increase in binding to *RBL1* (Fig. 4J and fig. S4F) and only a trend toward increased Rb binding for *PCNA* and *MYB* in both PDAC cell lines (Fig. 4, K and L, and fig. S4, G and H). Notably, the misp53^{R273H} ChIP-seq motif enrichment analysis indicated binding to motifs of the repressor E2F protein E2F4 (Fig. 2D), suggesting potential involvement of alternative cell cycle repression mechanisms mediated by key members of the DREAM complex (e.g., RBBP4 and E2F4) (*40*, *42*). To investigate whether misp53^{R273H} physically interacted with the cell cycle repressor protein E2F4, we conducted additional Co-IP experiments and found a marked protein-protein interaction between E2F4 and misp53^{R273H} (Fig. 4M). Subsequently, we performed E2F4 ChIP analysis in misp53$^{R273H/C}$ silenced cells (fig. S4, D and I) and observed that the loss of misp53$^{R273H/C}$ facilitated E2F4 binding to the promoters of cell cycle activator genes such as E2F1, RBL1, and proliferating cell nuclear antigen (PCNA) in both established and PDX cell lines (Fig. 4, N to P, and fig. S4, J to L). These results strongly indicate that

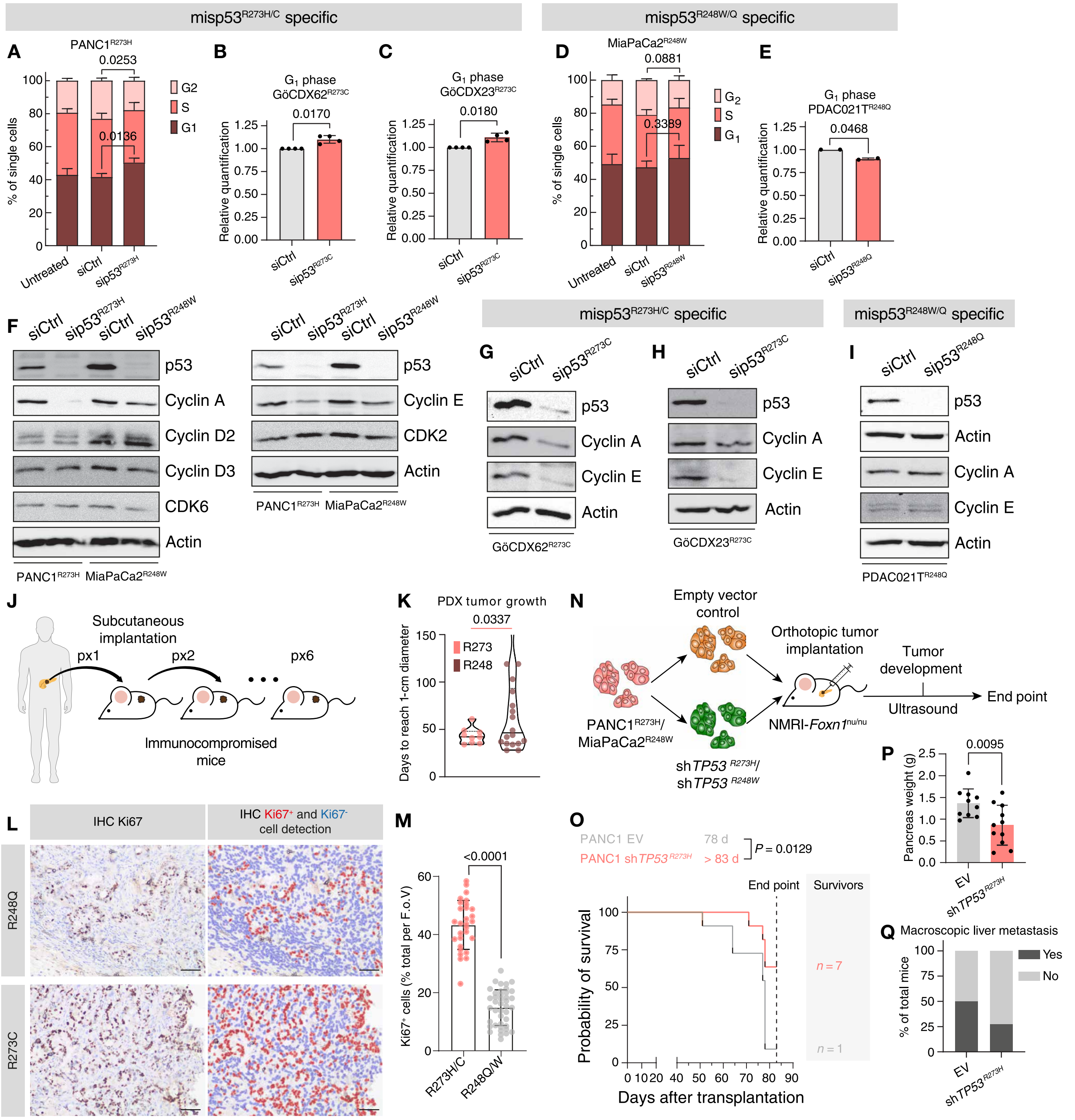

Fig. 3. Loss of misp53$^{R273H/C}$ leads to cell cycle arrest. (**A** and **D**) Cell cycle analysis of PANC1 and MiaPaCa2 cells after p53 silencing compared to control and untreated samples. *P* values and the percentage of single cells with means ± SD are shown ($n = 3$). (**B**, **C**, and **E**) Analysis of G1 phase after silencing misp53^{R273C} or misp53^{R248Q} (in red) compared to control siRNA (gray) in PDX cell lines [$n = 4$ for (B) and (C); $n = 2$ for (E)]. *P* values and relative number of single cells in G_1 phase with means ± SD are shown. (**F**) Immunoblot for cyclins, CDKs, and p53 after silencing p53 versus control ($n = 3$). (**G** to **I**) Immunoblot analysis in the indicated PDX cells for p53, cyclin A/E, and β-actin ("Actin") after p53 silencing [$n = 3$ for (G) and (H); $n = 2$ for (I)]. (**J**) Mice were subcutaneously implanted with primary PDAC tumors with either misp53$^{R273H/C}$ or misp53$^{R248Q/W}$ mutations. (**K**) Analysis of tumor growth rate of (J) is shown in violin plots. Each dot represents the number of days until the tumor achieved a diameter of 1 cm, with R273H/C tumors ($n = 2$) and R248Q/W tumors ($n = 4$). (**L**) Ki67 staining of tumors of (J), with Ki67$^+$ (red) and Ki67$^-$ (blue) cell detection shown (scale bar, = 200 μm). (**M**) Quantification of (L) for percentages of Ki67$^+$ cells per field of view (F.o.V.). Each dot represents one F.o.V., with $n = 2$ per condition. (**N**) Mice received orthotopic transplants of PANC1 or MiaPaCa2 cells with stable knockdown of *TP53* (sh*TP53*^{R273H} and sh*TP53*^{R248W}, respectively), or empty vector (EV) control. (**O**) Kaplan-Meier analysis of the PANC1 cohort indicates median survival, assessed using the log-rank test. (**P**) Pancreas weight measurements in PANC1 cohort ($n = 10$ for EV; $n = 11$ for sh*TP53*^{R273H}). (**Q**) Macroscopic analysis of liver metastasis for PANC1 EV and sh*TP53*^{R273H}. (A) to (E), (K), (M), and (P) used Student's *t* test with Welch's correction for statistical analysis.

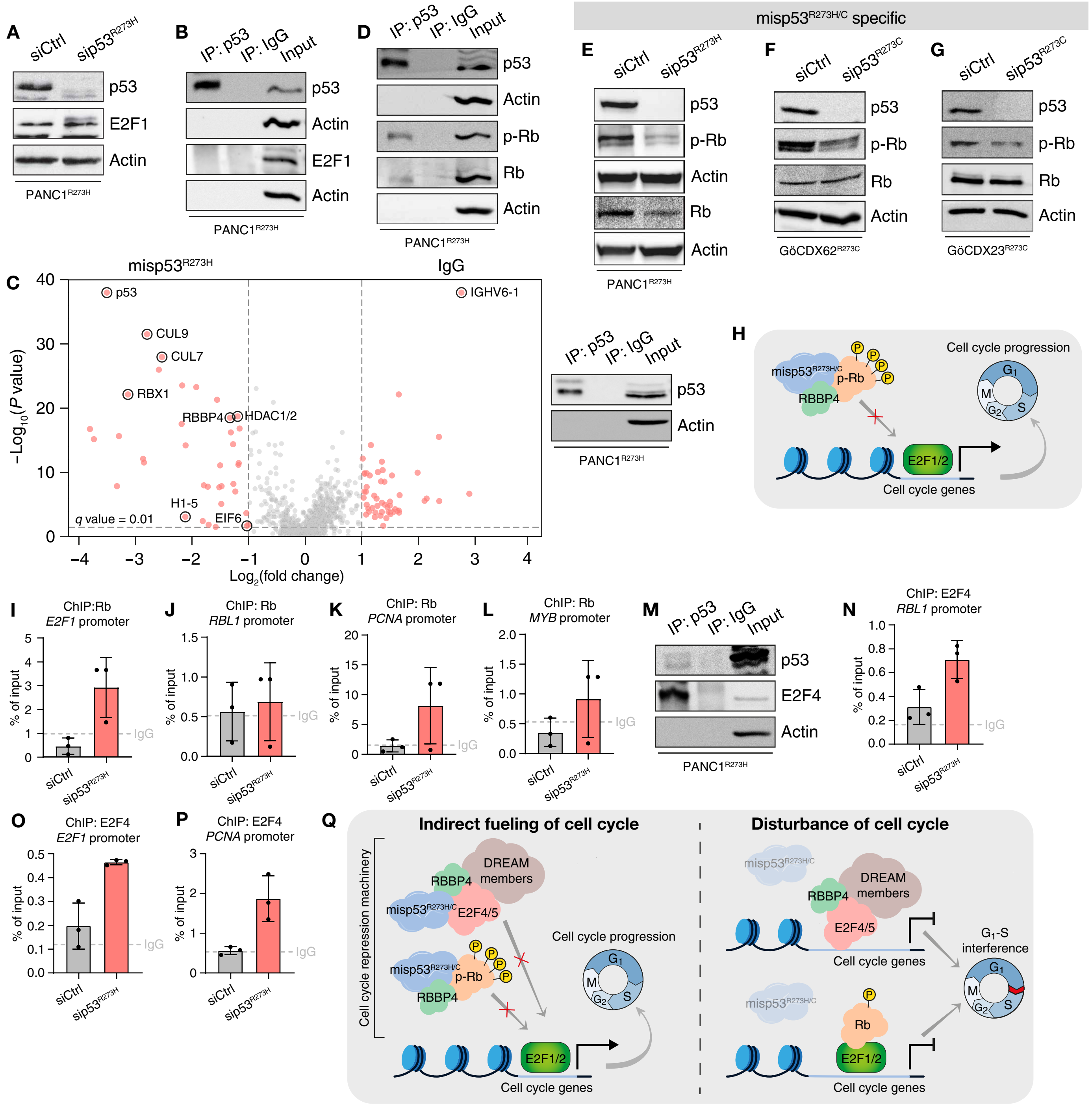

Fig. 4. Misp53$^{R273H/C}$ facilitates cell cycle progression by interacting with p-Rb and E2F4. (**A** and **B**) Immunoblot analysis for p53, E2F1, and β-actin (Actin) upon p53 silencing versus control siRNA (A) and after p53 pulldown, immunoglobulin G (IgG) isotype control, or input (B) in PANC1. $n = 3$ each. (**C**) Volcano plot showing the log$_2$(fold change) and the $-\log_{10}$(*P* value) comparing misp53^{R273H} pulldown to IgG control as determined by mass spectrometry analysis in PANC1. Red dots highlight candidates with a log$_2$(fold change) < -1 or > 1 and *q* value <0.01. Representative control immunoblot for p53 and Actin after p53 pulldown, IgG, or input. $n = 4$. (**D** to **G**) Immunoblot analysis for p53, p-Rb, Rb, and Actin after p53 pulldown, IgG, or input in PANC1 (D), upon sip53^{R273H} versus siCtrl in PANC1 (E) or sip53^{R273C} versus siCtrl in the PDX cell lines GöCDX62 (F) and GöCDX23 (G). $n = 3$ each. (**H**) Model of misp53$^{R273H/C}$ interaction with RBBP4 and phosphorylated p-Rb facilitating cell cycle progression. (**I** to **O**) ChIP qRT-PCR in PANC1 upon sip53^{R273H} versus siCtrl showing signal relative to input for Rb pulldown with means ± SD and average IgG isotype control over E2F1 promoter (I), RBL1 promoter (J), PCNA promoter (K), and MYB promoter (L). $n = 3$ each. (M) Immunoblot analysis for p53, E2F4, and Actin after p53 pulldown, IgG, or input in PANC1. $n = 3$. (N) to (**P**) ChIP qRT-PCR in PANC1 showing signal relative to input for E2F4 pulldown with means ± SD and average IgG isotype control over RBL1 promoter (N), E2F1 promoter (O), and PCNA promoter (P). $n = 3$ each. (**Q**) Model of misp53$^{R273H/C}$-mediated cell cycle progression.

misp53$^{R273H/C}$ interacts with the cell cycle repression machinery (e.g., p-Rb and E2F4), thereby regulating cell cycle progression. In the absence of misp53$^{R273H/C}$, cell cycle repressor proteins (e.g., p-Rb) inhibit cell cycle genes, leading to cell cycle arrest in the G_1 phase (Fig. 4Q). Therefore, targeting the cell cycle program associated with misp53$^{R273H/C}$ using established pharmacological inhibitors could be an effective approach for PDAC.

Loss of misp53$^{R273H/C}$ activates the MAPK/ERK signaling pathway

A previous study revealed that PDAC with aberrant G_1-S cell cycle transition could be effectively treated with the CDK4/6 inhibitor palbociclib (*43*). On the basis of our findings (as shown in Fig. 3 and Fig. 4), we investigated whether palbociclib treatment could effectively block misp53$^{R273H/C}$-mediated cyclin A/cyclin E–associated G_1-S cell cycle transition in PDAC. Of note, the effect of CDK4/6 inhibition on the expression levels of misp53 mutants in PDAC is currently unknown. We found that palbociclib substantially reduced the levels of misp53^{R273} in a dose-dependent manner (fig. S5, A and B) compared to misp53^{R248} (fig. S5, C and D). We then examined the effects of palbociclib on misp53^{R273H} as well as cyclin A and cyclin E levels. Our results showed that palbociclib caused a marked decrease in misp53^{R273H}, cyclin A, and cyclin E expression on both protein and mRNA levels (Fig. 5A and fig. S5E). This effect resembled the misp53$^{R273H/C}$-loss phenotype (Fig. 3, F to H), indicating that the CDK4/6 inhibitor palbociclib effectively reduced the levels of cyclin A and cyclin E, thereby inhibiting the G_1-S transition by decreasing misp53$^{R273H/C}$. To evaluate whether the therapeutic effectiveness of palbociclib was increased in misp53^{R273H}-depleted PDAC cells, we analyzed the efficacy of palbociclib in both EV and sh*TP53*^{R273H} cell lines. We observed that palbociclib reduced the cell viability of both EV and sh*TP53*^{R273H} cell lines in a dose-dependent manner (Fig. 5B). However, it was unexpected that the loss of misp53^{R273H} did not effectively decrease viability upon palbociclib treatment compared to EV. This suggests that PDAC cells may activate compensatory pathways in response to palbociclib treatment and in the absence of the misp53 protein. Of note, a recent study has shown that the therapeutic potential of palbociclib in PDAC is limited by the induction of MAPK/ERK signaling (*44*). This compensatory pathway can circumvent cell death and restore cell cycle progression in PDAC cells, potentially allowing them to survive the CDK4/6 inhibitory effect or the loss of misp53$^{R273H/C}$ (*44*, *45*). We also observed an increased phosphorylation of ERK (p-ERK) along with misp53^{R273H} reduction upon palbociclib treatment, indicating MAPK/ERK compensatory pathway in fueling cell cycle progression (Fig. 5C). However, it is yet to be determined how misp53$^{R273H/C}$ is involved in palbociclib-mediated cellular MAPK/ERK compensation in cell cycle progression and PDAC growth. Drug removal in palbociclib-treated PDAC cells (fig. S5F) revealed the restoration of misp53^{R273H} and its associated cyclin A/E levels, along with the phosphorylation of Rb, 24 hours post-washout (Fig. 5D). This was accompanied by a decrease in p-ERK levels 24 hours post-washout as compared to the 24-hour treatment group (Fig. 5D). This led us to investigate whether the deficiency of misp53$^{R273H/C}$ directly compensates via the MAPK/ERK pathway. We found that the levels of p-ERK and ERK1 transcripts were notably higher in misp53$^{R273H/C}$-deficient PDAC cell lines (Fig. 5, E to G). Furthermore, we observed elevated p-ERK levels in conjunction with a reduction in CK19^{+}p53^{+} tumor cells (Fig. 5, H and I, and fig. S5, G and H) in sh*TP53*^{R273H}-derived orthotopic tumors that reached end point criteria (Fig. 3, N and O). These findings strongly suggest that (i) loss of misp53$^{R273H/C}$ results in increased levels of MAPK/ERK pathway components and (ii) MAPK/ERK signaling compensates for palbociclib treatment in misp53$^{R273H/C}$ PDAC cells.

Targeting the MAPK/ERK pathway impedes misp53$^{R273H/C}$- and palbociclib-induced oncogenic compensation

To analyze the spatial distribution of p-ERK and misp53$^{R273H/C}$, as well as their mutual expression in the neoplastic compartment of PDAC tumors, we performed a multiplex-imaging study of orthotopic tumors derived from sh*TP53*^{R273H}. We used whole-slide images for immunofluorescence (IF) for CK19 (neoplastic cells) and p53 (Fig. 6A) and immunohistochemistry (IHC) for p-ERK (Fig. 6B) in serial sections and identified "hotspot" regions for either high p-ERK^{+} or high CK19^{+}p53^{+} tumor cell count. We found reduced p-ERK^{+} cells in p53^{+} hotspots and vice versa, substantially low CK19^{+}p53^{+} cells in p-ERK^{+} hotspots (Fig. 6C). These results strongly supported the idea that MAPK/ERK-mediated oncogenic adaptation was increased in misp53^{R273H} low PDAC. We investigated whether blocking the MAPK/ERK pathway with trametinib, a potent MEK1/2 inhibitor, impeded this adaptation. We found that trametinib treatment substantially reduced ERK phosphorylation in response to misp53^{R273H} silencing in PDAC cells (Fig. 6D), confirming that the MAPK/ERK pathway acted as an oncogenic compensatory pathway in misp53$^{R273H/C}$ deficiency, which could be inhibited by MAPK/ERK pathway inhibition. Therefore, a combination of the misp53$^{R273H/C}$-specific GOF inhibitor palbociclib and the compensatory MAPK/ERK signaling inhibitor trametinib seemed likely to be effective in treating misp53$^{R273H/C}$-specific PDAC. To test this, we treated misp53^{R273H}-specific PDAC cells with palbociclib, trametinib, or a combination of both drugs. Our study demonstrated that the combination treatment effectively reduced levels of misp53^{R273H} and the associated expression of cyclin A/E, while concurrently inhibiting the induction of p-ERK (Fig. 6E). To evaluate the efficacy of the palbociclib and trametinib combination in inhibiting PDAC cell growth, we performed drug synergy experiments on both established cell line (PANC1^{R273H}) and rapidly proliferating PDX cells (PDAC035T^{R273H}; Fig. 6, F and G). These two cell line models were used to assess tumor growth, metastasis, and disease aggressiveness via in vivo studies (Fig. 3, J to Q). Our results indicated that the combination of palbociclib and trametinib substantially reduced PDAC cell growth compared to individual treatments in both misp53^{R273H}-specific established and PDX cell lines (Fig. 6, F and G). Notably, our in vitro findings align well with previous studies, demonstrating that the combination of palbociclib and trametinib effectively blocks cell proliferation in PDAC preclinical models (*46*). Thus, using a combination of palbociclib and targeting the compensatory MAPK/ERK signaling pathway in misp53$^{R273H/C}$-specific PDAC may improve clinical outcomes.

DISCUSSION

Intratumoral plasticity is a crucial state that makes tumor cells challenging to both standard and targeted therapies. This plasticity enables PDAC tumors to grow even in an unfavorable environmental condition, such as exposure to therapeutic pressure. The presence of oncogenic mutations (e.g., in the *TP53* gene) drives distinct biological programs that help PDAC cells survive under these circumstances. However, the mechanisms by which PDAC cells use GOF

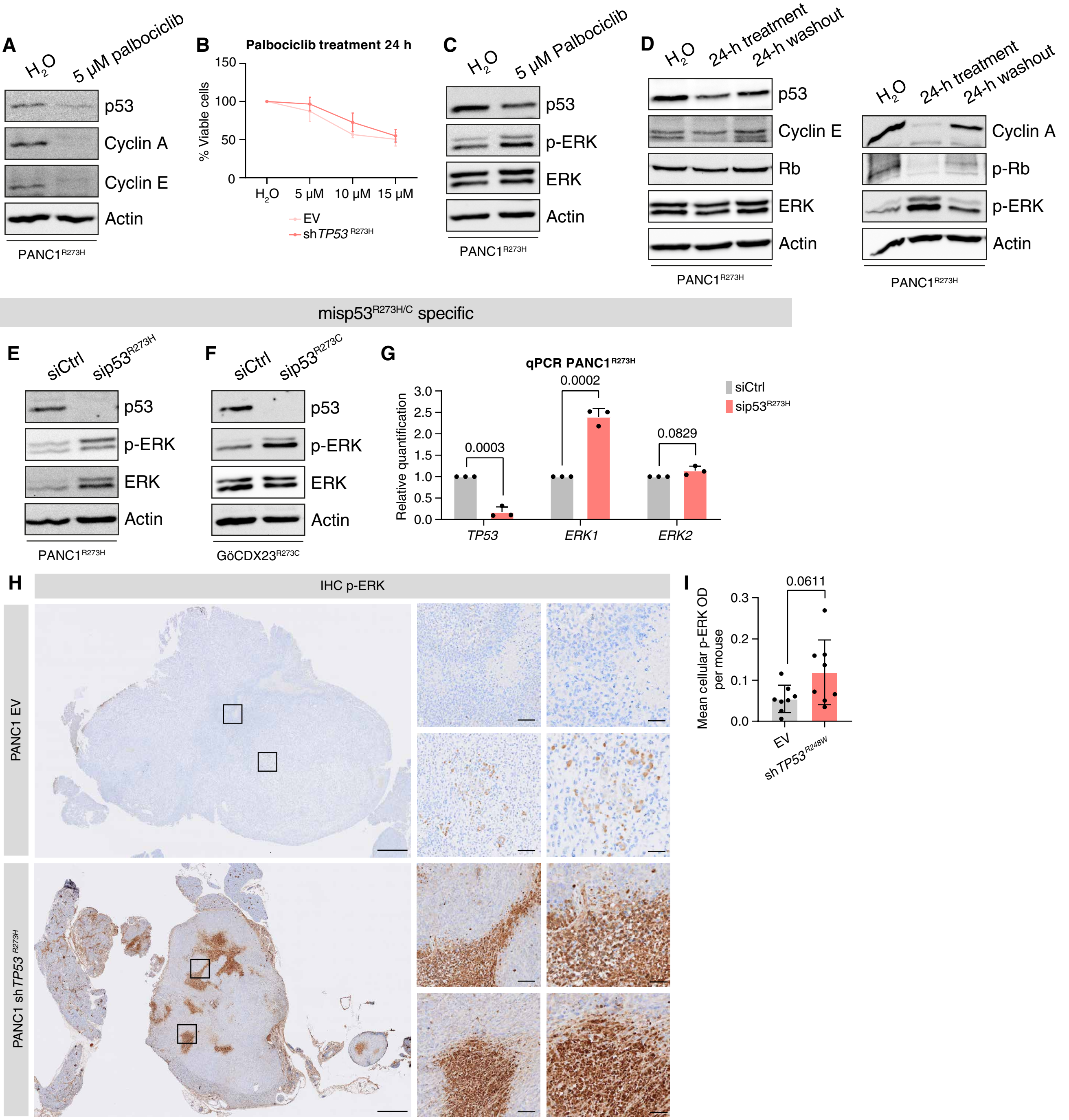

Fig. 5. Loss of the misp53$^{R273H/C}$ mutant results in the activation of the MAPK/ERK compensatory pathway. (**A**) Immunoblot analysis for p53, cyclin A, cyclin E, and β-actin (Actin) after 24 hours of 5 μM palbociclib treatment in PANC1. *n* = 3. (**B**) Cell viability in PANC1 with EV control and stable misp53^{R273H} knockdown (sh*TP53*^{R273H}) upon palbociclib treatment for 24 hours. Relative viability (to control) with means ± SD shown. *n* = 3 per condition. (**C**) Immunoblot analysis for p53, p-ERK, ERK, and Actin upon H_2O control or after 24 hours of 5 μM palbociclib treatment in PANC1. *n* = 3. (**D**) Immunoblot analysis for p53, cyclin A, cyclin E, p-Rb, Rb, p-ERK, ERK, and Actin upon H_2O control, 24-hour treatment with 5 μM palbociclib or 24-hour palbociclib followed by 24-hours washout in PANC1 cells. *n* = 3. (**E** and **F**) Immunoblot analysis for p53, p-ERK, ERK, and Actin after misp53$^{R273H/C}$ silencing (sip53$^{R273H/C}$) versus siCtrl in PANC1 (E) and GöCDX23 (F). *n* = 3 each. (**G**) qRT-PCR analysis for the indicated target genes in sip53^{R273H} (red), normalized to siCtrl (gray) in PANC1. Relative mRNA expression with means ± SD shown. *n* = 3 per condition and target. (**H**) IHC staining for p-ERK in PANC1 EV and sh*TP53*^{R273H} tumors. Scale bars, 1 mm (tumor overview), 100 μm (left), and 50 μm (right). (**I**) Quantification of (H). Mean cellular p-ERK optical density per mouse ± SD shown. *n* = 8 per condition. [(G) and (I)] Student's *t* test with Welch's correction was used to determine the *P* values. h, hours.

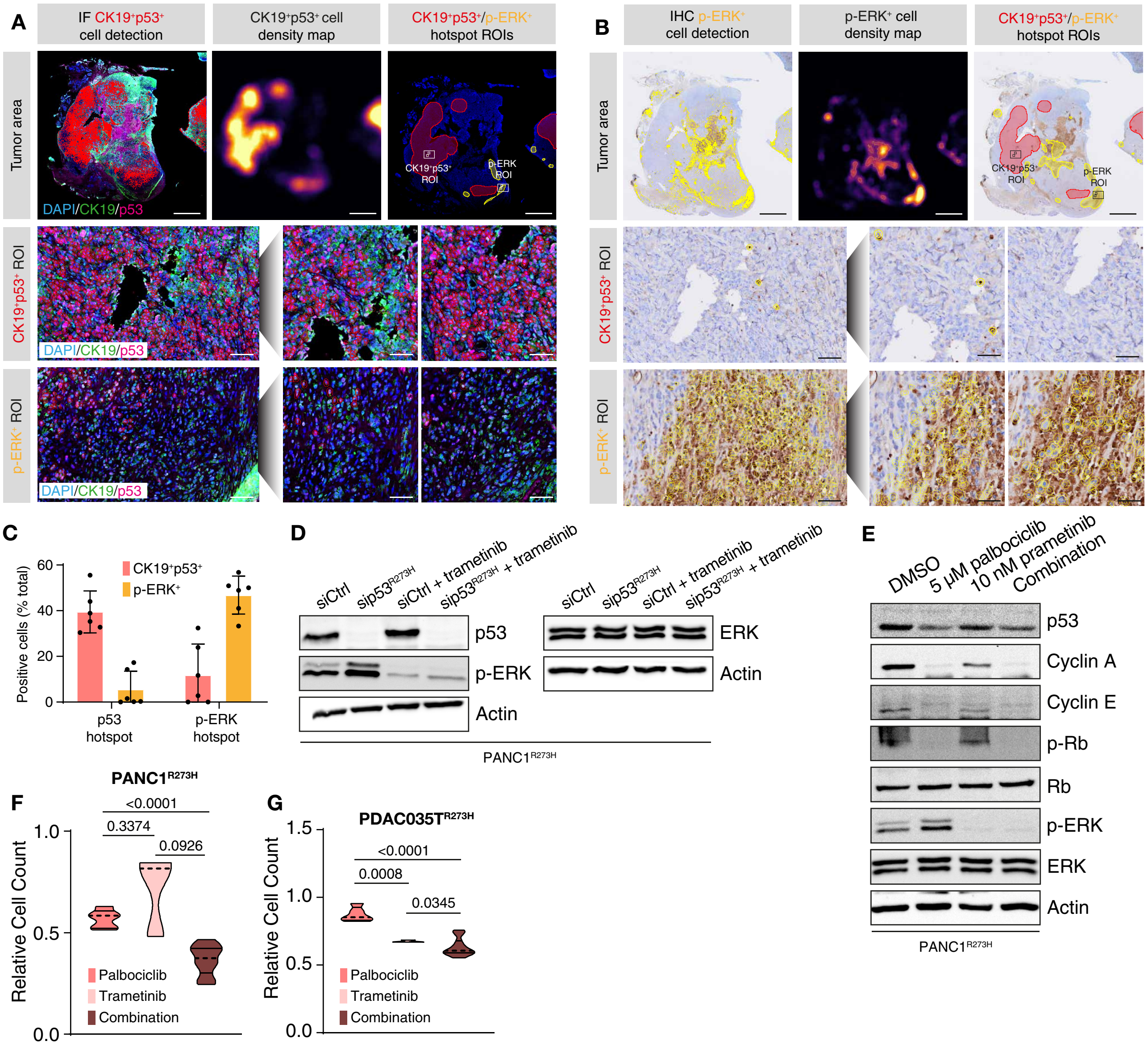

Fig. 6. Combined inhibition of ERK and CDK4/6 effectively counteracts the compensatory mechanism triggered by the loss of misp53$^{R273H/C}$. (**A** and **B**) Orthotopic PANC1 tumors (see Fig. 3N) were stained in serial sections for p53 and CK19 (A) and p-ERK (B) using IF and IHC, respectively. The positive cell detections for CK19^{+}p53^{+} and p-ERK^{+} are indicated in red and yellow, respectively. Density maps of positive cells were created and thresholded to obtain hotspot regions for CK19^{+}p53^{+} and p-ERK^{+} cells in the same tumors. Whole-tumor overviews (top) as well as a CK19^{+}p53^{+} (mid) and a p-ERK^{+} (bottom) regions of interest are shown. Scale bars, 2 mm (tumor overview), 100 μm (left zoom panels), and 50 μm (right zoom panels). (**C**) Quantification of CK19^{+}p53^{+} and p-ERK^{+} cells relative to the total number of detected cells in the hotspot regions with means ± SD shown. *n* = 6 per condition. (**D**) Immunoblot analysis for p53, p-ERK, ERK, and β-actin (Actin) after misp53^{R273H} silencing versus control siRNA or combination of sip53^{R273H} and 10 nM trametinib treatment versus siCtrl with DMSO in PANC1. *n* = 3. (**E**) Immunoblot analysis for p53, cyclin A, cyclin E, p-Rb, Rb, p-ERK, ERK, and Actin upon 5 μM palbociclib, 10 nM trametinib or the combination of both for 24 hours versus DMSO control in PANC1. *n* = 3. (**F** and **G**), Mean relative cell numbers after 72-hour treatment with either palbociclib (2.5 to 12.5 μM), trametinib (10 to 30 nM), or the combination in PANC1 (F) and PDAC035T (G). Values were normalized to control DMSO conditions. *n* = 3. Student's *t* test with Welch's correction was used to determine the *P* values.

missense p53 mutants (misp53) to keep growing under selective pressure are not fully understood. In this study, we investigated how transcriptional reprogramming driven by two different misp53 mutants affected cellular adaptability, tumor plasticity, and their potential role in targeted therapy for PDAC.

More than 70% of patients with PDAC carry *TP53* mutations, which is often linked to patients with poorly prognosed BL PDAC (*9*, *10*, *12*). Specifically, GOF misp53 mutants are associated with poor outcomes compared to non-GOF p53 mutants in patients with PDAC (*17*). Previous studies have shown that the loss of p53 function increases the plasticity of pancreatic cells (*47*), while GOF mutants like p53^{R172H} are correlated with increased disease aggressiveness and distant metastasis in comparison to p53-null cohorts, as observed in genetically engineered mouse models (*26*, *47*, *48*). Our study focuses on two key DNA contact mutants, namely misp53$^{R273H/C}$ and misp53$^{R248Q/W}$, which are present in around 3.1 and 2.8% of patients with PDAC, respectively (*9*, *23*, *28*, *29*). How these two hotspot mutations contribute to the PDAC plasticity and therapy response is largely unclear. Our findings suggest that the misp53$^{R273H/C}$ mutant promotes BL/EMT plasticity by fueling cell cycle progression and tumor growth in both in vitro and preclinical models. We also observed non–cell cycle–associated transcriptome signatures upon loss of misp53$^{R248W/Q}$, highlighting the heterogeneous functions of these two misp53 mutants. This underlines the specificity of misp53 mutants in regulating distinct transcriptional programs and that molecular functions vary depending on the location of their mutated codons.

Patient transcriptome data from TCGA (*28*) and QCMG (*9*), along with our genome-wide ChIP-seq analysis, indicate that GOF misp53$^{R273H/C}$ mutants are strongly associated with increased cell cycle signatures such as E2F targets, G_2-M checkpoint, and mitotic spindle. These results are especially important as a previous study has shown that mutations of cell cycle regulatory genes and cell cycle progression are elevated in patients with therapy-resistant, advanced-stage PDAC (*8*, *13*). In our preclinical studies, we have observed that misp53^{R273H}-deficient tumors display reduced growth and liver metastases in comparison to the misp53^{R248W}-deficient cohort. This suggests that misp53 mutants have different impacts on tumor plasticity and the advancement of subtype-specific disease through unique transcriptional programs.

Previous studies have shown that WT p53 is crucial in suppressing tumor formation by regulating cell cycle progression through the Rb/E2F and the Rb/DREAM/E2F signaling pathways (*40*, *42*). Our findings indicate that the misp53$^{R273H/C}$ mutant disrupts the tumor suppressor functions of Rb-E2F4 signaling axis, thereby promoting cell cycle progression in PDAC. We identified a unique mechanism where the loss of misp53$^{R273H/C}$ leads to the dephosphorylation of Rb (p-Rb), which in turn, inhibits E2F-mediated cell cycle progression. In addition, in misp53$^{R273H/C}$-silenced PDAC cells, the cell cycle repressor E2F4, an integral component of the DREAM complex, plays a key role in repressing genes that facilitate cell cycle progression. The DREAM complex enables this repression by assembling the MuvB subunit, which contains RBBP4, along with Rb-like proteins (p107 and p130) and the E2F repressor proteins E2F4 and E2F5 (*37*, *42*). It remains to be elucidated whether the misp53$^{R273H/C}$ mutant promotes E2F-mediated cell cycle progression solely by sequestering p-Rb or if other key components of the DREAM and RBBP4 complexes are also involved. Nonetheless, our findings suggest that the misp53$^{R273H/C}$ mutant actively contributes to cell cycle progression through the Rb-mediated repressor complexes. Our study aligns with previous research showing that misp53 mutant (e.g., misp53^{R175}) interacts with other oncogenic TFs or chromatin regulators (e.g., CREB1 or BRD4) to enhance PDAC aggressiveness (*21*, *22*, *49*). Our findings indicate that misp53$^{R273H/C}$ interacts with p-RB and E2F4, sequestering these factors, thereby promoting PDAC aggressiveness. Consequently, these misp53 mutant–specific interactions are crucial for the GOF activity of p53, distinguishing it from LOF mutants. Future studies using an isogenic cell system with specific mutants under appropriate allelic conditions are essential for fully elucidating the mechanisms that differentiate LOF and GOF p53 mutant functions in the plasticity of PDAC.

Clinically, pharmacological inhibition of p53 mutants in solid cancers remains a challenge. Efforts to target specific mutations in PDAC have not been successful, except for treating patients with *BRCA1/2* mutations (5% germline; 12% somatic), who can benefit from a combination of platinum-based chemotherapy and poly(adenosine diphosphate–ribose) polymerase inhibitors (*9*, *50*, *51*). However, on the basis of our results on misp53$^{R273H/C}$-mediated G_1-S cell cycle progression, we speculate that clinical CDK4/6 inhibitors (e.g., palbociclib) can be applied to target misp53$^{R273H/C}$-specific mutants. Treatment with palbociclib results in the down-regulation of misp53$^{R273H/C}$ and its associated cell cycle proteins, similar to the effect of silencing misp53$^{R273H/C}$. However, we also note that PDAC cells compensate for the loss of misp53$^{R273H/C}$ by activating the critical MAPK/ERK pathway, which is essential for PDAC cell survival. Our findings are supported by a recent study that shows that CDK4/6 inhibition induces ERK activation, which maintains PDAC cell proliferation (*44*). Together, these findings indicate that PDAC tumor cells adapt unique survival mechanisms upon the loss of misp53$^{R273H/C}$. This highlights the clinical challenge of potential therapeutic adaptation or resistance. In line, a previous study has shown that *TP53* mutations are associated with poor therapeutic response to CDK4/6 inhibitor treatment in patients with breast cancer (*52*). Therefore, we argue that understanding the molecular mechanisms of misp53$^{R273H/C}$-mediated plasticity and therapeutic adaptation can be useful for combining additional targeted therapies. Our findings indicate that combined targeting of the misp53$^{R273H/C}$ mutant specificity and the MAPK/ERK pathway with palbociclib and trametinib effectively counters compensatory cell proliferation mechanisms. Future work should aim to translate this combined pharmacological treatment approach to preclinical models. In addition, clinical studies that explore further targeting strategies within compensatory pathways to disrupt the effects of misp53$^{R273H/C}$ or the adaptations induced by CDK4/6 therapy are likely to provide important therapeutic options for PDAC.

In summary, our comprehensive study has delineated the mechanisms and functions of misp53 mutant specificity in PDAC plasticity and therapy response. These findings provide insights into the therapies based on molecular stratification in PDAC. The misp53$^{R273H/C}$ substantially contributed to cell cycle–dependent tumor growth and liver metastasis. Inhibiting misp53$^{R273H/C}$-specific GOFs using the CDK4/6 inhibitor leads to the activation of MAPK/ERK-mediated compensatory pathways, creating a therapy-induced adaptation in PDAC. Combining palbociclib with the MEK1/2 inhibitor trametinib reduces PDAC cell growth by antagonizing misp53$^{R273H/C}$-specific functions and MAPK/ERK-mediated adaptive mechanisms. Therefore, targeting misp53 mutants and their compensatory mechanisms has the potential to improve tailored treatment responses in PDAC.

MATERIALS AND METHODS

Preclinical in vivo studies

Orthotopic animal experiments were performed at the UMG in concordance with the guidelines of the Central Animal Experimental Authority (permission no. 21/3812). The ethics committee of the UMG also approved the generation of the PDX mouse models (permission no. 70112108). Orthotopic transplantation was performed on 9-week-old male NMRI-*Foxn1*$^{nu/nu}$ mice (Janvier Labs) by injecting a total of 1×10^6 cells (PANC1 EV, PANC1 sh$TP53^{R273H}$, MiaPaCa2 EV, and MiaPaCa2 sh$TP53^{R248W}$) suspended in 15 μl of respective cell culture medium into the pancreas under isoflurane anesthesia. Tumor development and growth were monitored through biweekly ultrasound examinations conducted under isoflurane anesthesia from the time point when the first tumors were palpable. The studies were terminated either 8 weeks after the ultrasound-confirmed detection of tumors or upon reaching predefined exclusion criteria, such as a body weight loss >20%, tumor volume >1000 mm^3, or the presentation of overall poor clinical conditions. For histological analysis, tissues were fixed in 4% (v/v) formalin and subsequently embedded in paraffin blocks.

Patient data analysis and study approval

This study analyzed patient tumors using publicly available datasets (*9*, *28*, *29*) for mutational and gene expression analyses. In addition, the data were generated from patients with PDAC enrolled in the study section of the KFO5002 and the Molecular Pancreatic Cancer Program (MolPac) at the UMG, as part of the study "Clinical and Molecular Evaluation of Patients with Pancreatic Lesions within the framework of the Pancreatic Program of the UMG" (ethics approval 11/5/17).

Data acquisition

TCGA (*28*), QCMG (*9*), and ICGC (*29*) were accessed via cBioPortal (*23*, *53*). KFO5002 primary tumor samples from resected patients were obtained in the Institute of Pathology at the UMG and used for Formalin-Fixed Paraffin-Embedded (FFPE) processing and generation of translational PDAC models (e.g., see primary PDAC cells from PDXs) and were subjected to DNA isolation using DNeasy Blood & Tissue Kit (Qiagen) following the manufacturer's protocol. Genetic characterization of tissue and models was conducted at the Institute of Human Genetics (UMG) using multigene panel sequencing. Briefly, 200 ng of genomic DNA were isolated, and library preparation was carried out using SureSelectTMXTHS and QXT target enrichment Kit (Agilent Technologies) with enzymatic fragmentation according to the manufacturer's instructions. Sequencing was run on an Illumina NextSeq550 with 2.5 high-output chemistry and 150–base pair (bp) read length. For read alignment to the human reference genome hg19 (Ensembl) and subsequent variant calling, Sequence Pilot Software (jsi medicalsystems GmbH) was used. Assessment of likely pathogenic and pathogenic variants followed the American College of Medical Genetics guidelines (*54*). Last, data were accessed via an internal KFO5002 cBioPortal platform. The generation of these data and the molecular characterization of the translational models were approved by the ethical review board of the UMG (8/1/17).

Data analysis

TP53 status–dependent gene expression analysis on TCGA and QCMG patient data was performed using the publicly accessible mutational information and normalized RNA-seq counts of both cohorts. R v4.2.1 was used for the analysis. MSigDB Hallmark and Curated (C2) gene set scores were calculated using the GSVA package v1.46.0 (*55*) for each cohort individually.

PDX mouse models and cell lines

Cell lines with the designation "GöCDX00," derived from PDX mouse models, were established from surgically resected PDAC tissues (*33*). These tissues were obtained from patients at the Ruhr-University Bochum Comprehensive Cancer Center (GöCDX62) and the UMG (all other GöCDX cell lines). Approval was granted by the ethics committee of Ruhr-University Bochum (permission no. 3534-9/3841-10/16-5792) and the UMG (permission no. 70112108). In addition, cell lines designated "PDAC000T" were created as previously described (*56*, *57*). Briefly, the PDAC specimens for these lines were collected either through surgical procedures or via endoscopic ultrasound-guided fine needle aspiration. The specimens were then implanted subcutaneously in the upper flank of NMRI-nude mice, following established methodologies (*57*). Each sample was combined with 100 μl of Matrigel (BD Biosciences, Franklin Lakes, NJ) and injected into the flank of a male nude mouse (Swiss Nude Mouse Crl:NU(lco)-Foxn1nu; Charles River Laboratories, Wilmington, MA) for initial implantation. Once the xenografts reached a volume of 1 cm^3, they were excised and transplanted into NMRI-nude mice using the same technique. PDAC samples were collected from three expert clinical centers as part of the PaCaOmics clinical trial (number 2011-A01439-32), following ethics review board approval. Informed consent forms were collected from patients and registered in a central database. Furthermore, all animal experiments were conducted in accordance with institutional guidelines and were approved by the "Plateforme de Stabulation et d'Expérimentation Animale" (Scientific Park of Luminy, Marseille, France).

Human cell culture

Established human PDAC cell lines PANC1 (RRID:CVCL_0480), MiaPaCa2 (RRID:CVCL_0428) and L3.6 [RRID:CVCL_0384; subclone (*58*) of Colo-357 (*59*)] were purchased from American Type Culture Collection (ATCC; Manassas, VA) and authenticated by the German Collection of Microorganisms and Cell Cultures GmbH. PANC1 and MiaPaCa2 were cultured in Dulbecco's modified Eagle's medium (DMEM, high glucose, + L-Glutamine; Thermo Fisher Scientific) supplemented with 10% (v/v) fetal calf serum (FCS; Th. Geyer). L3.6 was cultured in minimum essential medium (MEM + L-Glutamine; Thermo Fisher Scientific) containing 10% (v/v) FCS. PDX-derived primary cell lines with the nomenclature GöCDX000 were maintained in a 3:1 mixture of Keratinocyte-SFM [Thermo Fisher Scientific; supplemented with 2% (v/v) FCS, 1% (v/v) penicillin-streptomycin (Sigma-Aldrich), bovine pituitary extract (25 mg/500 ml; Thermo Fisher Scientific), and human epidermal growth factor (25 ng/500 ml; Sigma-Aldrich)] and RPMI 1640 (high glucose, + L-Glutamine; Thermo Fisher Scientific) containing 10% (v/v) FCS. PDX-derived primary cell lines holding the nomenclature PDAC000T were cultured in serum-free ductal media as described by Schreiber *et al.* (*60*).

Generation of lentiviral transduced stable cell lines

TP53 short hairpin RNA (shRNA) constructs (#1: TRCN0000003755, #2: TRCN0000003753) with pLKO.1 backbone were purchased from Sigma-Aldrich. Envelope vector (pMD2.G; no. 12259), packaging vector (psPAX2; no. 12260), and EV control (pLKO.1; no. 10879) were purchased from Addgene. shRNA constructs and listed vectors were amplified in chemically competent *Escherichia coli* K12 derivates (Invitrogen). For virion production, 1×10^6 human embryonic kidney 293T/17 cells (ATCC) were seeded in culture dishes 24 hours before transfection. Transfection was performed using Lipofectamine 2000 (Invitrogen) and Opti-MEM (Thermo Fisher Scientific) according to the manufacturer's instructions in a 2:1.5:1 mixture with the respective shRNA construct (5 μg), the lentiviral packaging vector (3.75 μg), and the envelope vector (2.5 μg). Virus-containing supernatant was harvested, filtered through a 0.45-μm filter, and together with polybrene (0.8 μl/ml; Santa Cruz Biotechnology) added to the confluent target cell culture (PANC1, MiaPaCa2) for transduction. Following 24 hours of incubation, the cells were selected with puromycin (2 μg/ml; Sigma-Aldrich) for 72 hours and later maintained in DMEM (high glucose, + l-Glutamine; Thermo Fisher Scientific) supplemented with 10% (v/v) FCS (Th. Geyer) and puromycin (1 μg/ml). For downgrading from safety level S2 to S1, the cells underwent reverse transcription polymerase chain reaction (RT-PCR) for pMD2.G and psPAX2. In brief, viral RNA from cell culture supernatant was extracted using the Direct-zol RNA MiniPrep kit (Zymo Research) according to the manufacturer's instructions. cDNA and PCR reactions were performed using the OneTaq One-Step reverse-transcriptase PCR (RT-PCR) Kit (New England Biolabs) with instruction manual describing dilutions of the components, and the PCR scheme indicated in table S2. Amplified samples were run by a PowerPac HC (Bio-Rad) on a 1.5% agarose gel together with amplification products resulting from pMD2.G and psPAX2 plasmids as positive controls to validate virus depletion in the cell lines. Primer sequences used for amplification are listed in table S3.

siRNA transfection

For transient knockdown of the *TP53* transcripts, 3 to 5 × 10^5/3 ×10^6 cells per six-well/15-cm dish were seeded and directly transfected with a mixture of 10/95 μl of Lipofectamine 2000 (Thermo Fisher Scientific), 120/947 pmol of target-specific siRNA (s605, catalog 4390824, Thermo Fisher Scientific), and 200 μl/1.5 ml of Opti-MEM (Thermo Fisher Scientific) after 15-min incubation of the transfection mixture at room temperature (RT). The medium was changed 8 hours after transfection. Twenty-four hours after the first transfection, the cells underwent a second transfection, as described before. The cells were harvested for protein/RNA extraction or follow-up experiments 72 hours after the first transfection. All siRNA sequences are listed in table S3.

Transient overexpression of mutant p53

For transient overexpression of mutant p53, human $p53^{null}$ L3.6 cell line was used. First, 2.5 × 10^5 cells were seeded in six-well culture dishes and directly transfected with a mixture of 1.5 μl of Lipofectamine 2000 (Thermo Fisher Scientific), 4 μg of an enhanced green fluorescent protein control plasmid (pEGFP-C2, no.6083-1, Addgene) or 4 μg of the $p53^{R273H}$ carrying plasmid (pRc/CMV $p53^{R273H}$, Invitrogen), and 200 μl Opti-MEM (Thermo Fisher Scientific) upon 15-min incubation of the mixture at RT. The medium was changed 8 hours after transfection, and the cells were harvested 48 hours after transfection for protein extraction and analysis by immunoblotting.

Immunoblotting

Cells were washed twice with phosphate-buffered saline (PBS) and subsequently lysed in whole-cell lysis (WCL) buffer supplemented with cOmplete protease inhibitor cocktail (Roche Diagnostics), 1 mM sodium orthovanadate (NaO; Sigma-Aldrich), and 1 mM phenylmethylsulfonyl fluoride (PMSF; Sigma-Aldrich) for 1 hour on ice. Lysates were centrifuged at 17,000*g* for 30 min at 4°C to collect the supernatant of which protein concentration was determined via Bradford (Bio-Rad) assay. Proteins were diluted to equal concentrations between 0.8 and 1.0 μg/μl with WCL and Laemmli buffer and boiled for 8 min at 95°C. Denatured proteins were resolved via 10% (v/v) SDS–polyacrylamide gel electrophoresis (SDS-PAGE) and transferred onto nitrocellulose membranes in a semidry blotting system (Bio-Rad). Membranes were blocked with 5% (w/v) milk powder in tris-buffered saline with 0.1% (v/v) Tween 20 (Sigma-Aldrich) and subsequently incubated with primary antibodies at 4°C overnight. Secondary horseradish peroxidase (HRP)–linked antibodies were incubated at RT for 1 hours. Protein was detected by development with enhanced chemiluminesence solution (Bio-Rad) and imaging in an Intas ChemoCam Imager (Intas Science Imaging) and the associated ChemoStar Software (Intas Science Imaging). Antibodies are listed in table S4.

Co-IP and mass spectrometry analysis

Co-immunoprecipitation

Cells were seeded in 10-cm culture dishes and, upon reaching 80 to 90% confluency, harvested by scraping in 1 ml of ice-cold PBS. Cell suspension was centrifuged at 500*g* at 4°C for 5 min. Supernatant was discarded and pellet lysed in lysis buffer [200 mM NaCl, 50 mM tris (pH 8.5)] containing 1% (v/v) Triton X-100 (Sigma-Aldrich) for 30 min on ice. The lysates were centrifuged at 17,000*g* at 4°C for 20 min. Protein concentration of the supernatant was measured by Bradford (Bio-Rad) assay, and 500 μg of protein was added to 20 μl of washed agarose protein G beads (Merck Millipore) with 0.32 μg of normal mouse immunoglobulin G (IgG, sc-2025, Santa Cruz Biotechnology) for preclear. After 1 hour of incubation on a rotating wheel at 4°C, the beads were removed by centrifugation, discarded, and precleared lysates incubated with 5 μg of target antibody for p53 (sc-126 DO-1, Santa Cruz Biotechnology) or 0.6 μg of normal mouse IgG (sc-2025, Santa Cruz Biotechnology) as control on a rotating wheel at 4°C overnight. The next day, 50 μl of washed agarose G beads were added to the lysates for 2 hours of incubation on a rotating wheel at 4°C. The beads/antibody/target protein complexes were harvested by centrifugation and washed twice with WCL buffer, followed by two times washing with PBS with cOmplete protease inhibitor cocktail (Roche). Afterward, the complexes were resuspended in 65 μl of 2x Laemmli buffer and boiled for 8 min at 95°C. For targeted analysis, the samples were analyzed by immunoblotting as described above. To avoid heavy-chain signal of the antibody used for pulldown while imaging, the targets that were stained with primary antibodies from the same species were incubated with an anti–light-chain antibody raised in another species before using a secondary HRP-linked antibody. For mass spectrometry preparation, the samples were resolved via 10% (v/v) SDS-PAGE; the gel was then rinsed with double dH_2O and stained with Coomassie stain (Sigma-Aldrich) for 1 hour at RT. The stained gel was washed twice with double dH_2O and subsequently incubated in destain solution (20% methanol and 10% acetic acid) overnight at RT. The following day, the gel was imaged brightfield to assess protein content, afterward washed with double dH_2O for 1 hour at RT, and finally used for immunoblotting for target protein pulldown verification as described above. Antibodies are listed in table S4.

Mass spectrometry analysis

Protein samples were loaded onto 4 to 12% NuPAGE Novex bis-tris Minigels (Invitrogen) and run into the gel for 1.5 cm. Following Coomassie staining, the protein areas were cut out, diced, and subjected to reduction with dithiothreitol, alkylation with iodoacetamide, and finally overnight digestion with trypsin. Tryptic peptides were extracted from the gel, the solution dried in a Speedvac, and kept at −20°C for further analysis (*61*).

Samples were redissolved in 20 μl of loading buffer (2% acetonitrile and 0.1% trifluoroacetic acid in water) spiked with a synthetic peptide standard used for retention time alignment (iRT Standard, Schlieren, Switzerland) and analyzed on a nanoflow chromatography system (nanoRSLC, Thermo Fisher Scientific) hyphenated to a hybrid timed ion mobility–quadrupole-time-of-flight mass spectrometer (Pro 2, Bruker). In brief, 150 ng equivalents of peptides were enriched on a reversed-phase C18 trapping column (0.3 cm by 300 μm, Thermo Fisher Scientific) and separated on a reversed-phase C18 column with an integrated CaptiveSpray Emitter (Bruker PepSep MAX, 15 cm by 150 μm, IonOpticks) using a 13-min linear gradient of 5 to 35% acetonitrile/0.1% formic acid (v/v) at 850 nl/min and a column temperature of 50°C.

Data independent acquisition (DIA) analysis was performed in diaPASEF mode (*62*) using an 8 by 2 variable size window acquisition method from mass/charge ratio (*m/z*) 400 to 1200 to include the 2+/3+/4+ population in the *m/z*–ion mobility plane. The collision energy was ramped linearly as a function of the mobility from 59 eV at 1/K0 = 1.6 Vs/cm^2 to 20 eV at 1/K0 = 0.6 Vs/cm^2. Three technical replicates per biological replicate were acquired.

Protein identification was achieved using the Pulsar algorithm in Spectronaut Software v16.0 (Biognosys) using default settings. All DIA data were searched against the UniProtKB *Homo sapiens* reference proteome (revision 01-2021) augmented with a set of 51 known common laboratory contaminants at default settings. For quantitation, up to the 6 most abundant fragment ion traces per peptide and up to the 10 most abundant peptides per protein were integrated and summed up to provide protein area values. Mass and retention time calibration as well as the corresponding extraction tolerances were dynamically determined. Both identification and quantification results were trimmed to a false discovery rate of 1% using a forward-and-reverse decoy database strategy.

RNA isolation and qRT-PCR

RNA isolation

Cells were washed once with PBS, and total RNA was extracted using 800 μl of TRIzol reagent (Invitrogen) according to the manufacturer's instructions. After addition of 200 μl of chloroform, the cells were vortexed for 5 s and incubated for 5 min at RT followed by centrifugation at 17,000*g* for 15 min at 4°C for phase separation. The upper aqueous phase was then transferred to a fresh 1.5-ml tube, and 500 μl of isopropanol was added. After vortexing and incubation for 10 min at RT, the samples were again centrifuged at 17,000*g* for 30 min at 4°C to precipitate the RNA pellet. Next, the pellet was washed twice with 75% ethanol and finally dried and dissolved in 30 μl of nuclease-free water for storage until use at −80°C.

cDNA synthesis and qRT-PCR

cDNA was prepared using 1 μg of RNA and the iScript cDNA Synthesis Kit (Bio-Rad) according to the manufacturer's protocol. Quantitative real-time PCR (qRT-PCR) samples contained 5 μl of SYBR green (Bio-Rad), 0.25 μl of forward and reverse primers each, and 1 μl of cDNA. qRT-PCR was performed in 40 cycles on a StepOnePlus Real-Time System (Applied Biosystems), and relative quantification results were calculated with the StepOnePlus software (Applied Biosystems) with *XS13* as the reference control gene. Primer sequences are listed in table S3.

RNA-seq and data processing

PANC1 and MiaPaCa2 were seeded in six-well plates, subjected to siRNA knockdown for *TP53* transcripts, and RNA isolation was performed as detailed above. RNA quality measurement and cDNA library preparation were performed by the next-generation sequencing (NGS) service facility of the UMG (NIG). Briefly, RNA quality was determined by fragment analyzer (Agilent). The cDNA library was prepared using 1 μg of RNA and the TruSeq RNA Library Prep Kit v2 (Illumina). cDNA concentration was measured using the DeNovix dsDNA High Sensitivity Kit (Biozym Scientific GmbH) and the DeNovix Fluorometer (Biozym Scientific GmbH). Fragment sizes were confirmed by Fragment Analyzer (Agilent). Sequencing of nonstranded mRNA was performed on a HiSeq4000 (Illumina) generating 25 Mio single-end reads (50 bp) per sample. The raw reads were quality controlled using FastQC (*63*) v0.11.9 and checked for both microbial and mouse contamination using Kraken (*64*) v2.0.8 and FastQ Screen (*65*) v0.14.1, respectively. Next, the reads were trimmed using Trimmomatic (*66*) v0.39, then mapped to the human reference genome (Ensembl, genome assembly GRCh38.p13) using STAR (*67*) v2.7.7a, and, finally, features were quantified using HTSeq-Count (*68*) v2.0.1. All results were gathered into a comprehensive report using MultiQC (*69*) v1.10.1. Downstream analysis was performed using R v4.1.1 and Bioconductor (*70*) packages v3.15 on a High-Performance Computing (HPC) cluster of the corporation for scientific data processing (GWDG) in Göttingen, Germany. RUVSeq (*71*) v1.28.0 function RUVs was used to achieve variance stabilization followed by DESeq (*72*) v1.34.0 for differential gene expression analysis. GSEA (*73*) was performed with clusterProfiler (*74*) v4.2.2 and public signatures of the Molecular Signature Database (*75*) (MSigDB).

ChIP and ChIP qRT-PCR

Cells (10 to 15 × 10^6) on 15-cm culture dishes were cross-linked with 1% (v/v) paraformaldehyde (PFA, Thermo Fisher Scientific) in PBS for 20 min at RT followed by quenching of the reaction with 1.25 M ice-cold glycin (final concentration 0.125 M) for 5 min at RT. The cells were washed twice with ice-cold PBS and scraped in cooled modified Nelson buffer [150 mM NaCl, 20 mM EDTA (pH 8.0), 50 mM tris (pH 7.5), 0.5% NP-40, 1% Triton X-100, and 20 mM NaF] supplemented with cOmplete protease inhibitor cocktail (Roche), 1 mM NaO, and PMSF, and 10 mM NaF. Next, the cell suspension was centrifuged at 12,000*g* for 2 min at 4°C and washed once with Nelson buffer containing the aforementioned inhibitors. The resulting nuclear pellets were snap-frozen in liquid nitrogen and optionally stored at −80°C until further use. The pellets were lysed with Gomes lysis buffer [150 mM NaCl, 1% (v/v) NP-40, 0.5% (w/v) sodium deoxycholate, 50 mM tris-HCl (pH 8.0), 20 mM EDTA, and 20 mM NaF] supplemented with cOmplete protease inhibitor cocktail, 1 mM NaO and PMSF, and 10 mM sodium fluoride and 0.1% (v/v) SDS for 30 min on a rotating wheel at 4°C. The lysates were then sonicated with a Bioruptor Pico (Diagenode) for two to eight cycles in 15 to 30 s ON/OFF mode followed by a chromatin shearing check via agarose gel electrophoresis. Samples (300 to 500 bp sized) were precleared for 1 hour using 15 μl of washed protein A/G double-coated magnetic beads (Thermo Fisher Scientific) and, after removal of the beads, incubated with the pulldown antibodies or isotype controls overnight on a rotating wheel at 4°C. To collect the beads/protein/chromatin complexes, 30 μl of washed beads were added to the lysates and incubated for 2 hours at 4°C on a rotating wheel. Next, the lysates were washed once with Gomes lysis buffer, twice with Gomes wash buffer [100 mM tris-HCl (pH 8.5), 500 mM LiCl, 1% (v/v) NP-40, 1% (w/v) sodium deoxycholate, 20 mM EDTA, and 20 mM NaF], and followed by another two times with Gomes lysis buffer and one time with 1× TE buffer [pH 9.0; 10 mM tris-HCl (pH 7.4), 1 mM EDTA (pH 8.0)]. Input and pulldown samples were digested with ribonuclease A (RNAse A, Sigma-Aldrich) and proteinkinase K (AppliChem GmbH) and DNA isolated by phenol-chloroform-isoamyl alcohol method. Subsequent RT-qPCR was conducted as described above with increasing the number of cycles to 55. Results were normalized to input DNA. Antibodies are listed in table S4 and primer sequences in table S3.

ChIP-seq and data processing

Library preparation and data processing

ChIPs for the p53 mutants misp53^{R273H} and misp53^{R248W} in PANC1 and MiaPaCa2, respectively, were performed as described above. Two nanograms of immunoprecipitated DNA was used for library preparation with the Microplex Library Preparation Kit v3 (Diagenode) according to the manufacturer's instructions. cDNA concentration was determined with the Qubit dsDNA HS Assay Kit (Thermo Fisher Scientific) and the Qubit 3 Fluorometer (Thermo Fisher Scientific). Library integrity was verified with a 2100 Bioanalyzer (Agilent) and sequenced at the NGS service facility of the UMG (NIG) with an HiSeq4000 (Illumina) generating 25 Mio single-end reads (50 bp) per sample. Preprocessing and downstream analysis were conducted on an HPC cluster of the GWDG in Göttingen, Germany. Raw reads were quality controlled using FastQC (*63*) v0.11.4 and results gathered into a comprehensive report using MultiQC (*69*) v1.13. Next, raw reads were aligned to the human reference genome hg38 and cleared for duplicates using Bowtie2 (*76*) v2.3.4.1, SAMTools (*77*) v1.9, and BEDTools (*78*) v2.29.1. Peak calling was performed using MACS2 (*79*) v2.1.2.

Peak overlap and annotation

Downstream analysis was executed with R v4.1.1. Because of biological replicate restriction, only peaks with a q value $<10^{-10}$ were analyzed to strengthen relevance of the data. To identify misp53^{R273H}- and misp53^{R248W}-specific peaks, ChIPpeakAnno (*80*) v3.28.1 package was used. Misp53^{R273H}-specific peaks were defined as peaks not overlapping with misp53^{R248W} peaks and vice versa. Genomic annotation was plotted using the functions of ChIPseeker (*81*) v1.30.3 package. Occupancy heatmaps over TSS were generated with computeMatrix v3.2.0.0.0 and plotHeatmap v3.2.0.0.1 of deepTools (*82*) in Galaxy (*83*).

Motif analysis

To analyze motif enrichment, the AME function of MEME suite v5.5.0 was used. Misp53^{R273H}- and misp53^{R248W}-specific peaks were centered at their summits and extended to 200 bp. Next, the peaks were exported as FASTA files and ran in AME with shuffled input sequences as control. Motifs of the HOCOMOCOv11 core human set were applied and statistics reported by Fisher's exact test. Full results are in table S1.

Cell cycle phase analysis

For assessment of cell cycle phases upon siRNA-mediated knockdown, the cells were seeded in six-well culture dishes and transfected with siRNA for *TP53* as detailed above. Six hours after the second transfection, the cells were cultured in serum-free media for 18 hours for starvation. Release was mediated by a change to standard media compositions. After 72 hours upon the first transfection, the cells were harvested for flow cytometry.

To perform flow cytometry, the cells were harvested by washing with sterile PBS, detaching using 1× 0.5% Trpysin-EDTA (Thermo Fisher Scientific) and resuspending a maximum of 1×10^6 cells in 600 μl of PBS and transferring them to flow cytometry tubes (Sarstedt). Fixation was achieved by adding 1.4 ml of ice-cold ethanol in droplets while vortexing. The samples were incubated for at least 30 min at 4°C and afterward centrifuged at 266*g* for 10 min at RT. For propidium iodide (PI) staining, the cells were washed twice with PBS with 1-min incubation for rehydration each. After another centrifugation at 266*g* for 10 min at RT, the pellets were resuspended in 100 μl of PBS containing PI (0.05 μg/μl; Sigma-Aldrich) and RNAse A (0.005 μg/μl; Sigma-Aldrich) and incubated at 37°C for 30 min. Two hundred microliters of PBS per sample was added, and suspensions were filtered through 50-μm nonsterile Filcon cup (BD Biosciences) to reduce cell clumping. A total of 10,000 events per sample were measured in an LSRFortessa X-20 (BD Biosciences) flow cytometer and analyzed using FlowJo v10.1 software (BD Biosciences). Briefly, events were gated for living cells with forward scatter height (FSC-H) and side scatter height (SSC-H) and living cells for single cells using FSC-H andforward scatter area (FSC-A). Cell cycle analysis on the PI [PI(561)-A] signal histogram was conducted using the built-in cell cycle analysis tool of the FlowJo software with the Watson (pragmatic) model. Constraining of peaks was only performed when fitting of the model was insufficient. Gating strategy and curve fitting of the cell cycle analysis tool are shown in fig. S6. Knockdown of *TP53* transcription was confirmed by immunoblotting as described above.

Cell viability assay

The CellTiter-Glo Luminescent Cell Viability Assay (Promega) was used to determine cell viability upon treatment with palbociclib in the indicated dosages. In brief, 2×10^3 cells were cultured in 96-well culture plates 24 hours before treatment and underwent therapy for either 24 or 48 hours. Afterward, the cells were incubated at RT for 30 min and further with CellTiterGlo solution according to the manufacturer's protocol. Last, luminescence was measured with the LUmo luminometer (Autobio).

Cell proliferation and viability assay with live-cell imaging

To assess cell proliferation following treatment with palbociclib, trametinib, or a combination of both, PANC1 cells and PDAC035T cell lines were seeded at densities of 5×10^3 and 3×10^5 cells per 24-well plate, respectively, 24 hours before treatment. The cells were treated for 72 hours with palbociclib at five varying concentrations (ranging from 2.5 to 12.5 μM) and trametinib at three concentrations (ranging from 10 to 30 nM), administered either as single treatments or in combination. Throughout the treatment period, live-cell images were captured every 4 hours using the Incucyte SX5 (Sartorius), and the number of cells was quantified using standard Incucyte software. Mean relative cell numbers of three biological replicates after 72-hour treatments were normalized to control dimethyl sulfoxide (DMSO) conditions.

Treatment recovery experiments

The cells (7.5×10^4) were seeded in six-well culture dishes 24 hours before treatment and subsequently treated with 5 μM palbociclib for a total duration of 24 hours. For treatment recovery, confluent cells were washed several times with sterile PBS and received fresh media without the inhibitor for 24 hours. Eventually, the samples were lysed in WCL for protein extraction and further analysis via immunoblotting.

H&E staining and immunohistochemistry

Tissues were fixed in 4% (v/v) PFA, embedded in paraffin blocks, and cut in 4-μm-thick sections. Hematoxylin and eosin (H&E) staining was performed as described before (*33*). For IHC, the slides were stained according to a standard protocol on an Autostainer (Agilent). In brief, the specimens were deparaffinized in xylene and rehydrated in descending concentrations of ethanol. Antigen retrieval was performed at 95°C in pH 9.0 Envision FLEX target retrieval solution in a PT Link Module (Agilent). Next, the slides were incubated with primary antibody for 1 hour, washed with PBS, and incubated with an appropriate secondary antibody (EnVision Flex+, Dako) for 30 min. Antibody recognition was detected with peroxidase-conjugated goat anti-rabbit IgG secondary antibody (Cell Signaling Technology) at RT for 30 min. Subsequently, the slides were washed with 0.1 M PBS buffer (pH 7.4) and thus perceptible by the DAB (3,3′-diaminobenzidine) kit. Last, the sections were counterstained with hematoxylin. Used antibodies and their respective concentrations are listed in table S3.

Immunofluorescence

Tissues were fixed in 4% (v/v) PFA, embedded in paraffin blocks, and sectioned at a thickness of 4 μm. IF staining was performed as previously described (*33*). Antibodies are listed in table S3.

Image acquisition and analysis

Bright-field (H&E and IHC) and fluorescence (IF) imaging were performed with the Olympus VS200 virtual slide microscope (Olympus). Quantification was conducted using QuPath v0.5.0. For IHC images, cell detection was determined by hematoxylin optical density of the nuclei and positive cells were quantified by deconvoluted DAB intensity. These measurements provide positive cell count and DAB intensity per cell, per nucleus, or per cytoplasm for further analysis. For IF images, the built-in detection feature was used for cell detection according to the nuclear 4′,6-diamidino-2-phenylindole signal. Single- or double-positive cells were quantified with adjusted single or compound classifiers, respectively. From this, positive or double-positive cell count and staining intensity per cell, per nucleus, or per cytoplasm were exported for further analysis.

Statistical analysis

For statistical analysis, GraphPad Prism version 8.0.2 was used. Analysis of independent groups was performed using an unpaired Student's *t* test with Welch's correction. Survival data were compared using the log-rank (Mantel-Cox) test. Significance cutoff was set at a *P* value below 0.05, as indicated in the figures.

Supplementary Materials

This PDF file includes:
Figs. S1 to S6
Tables S1 to S4
Uncropped Western blots
References

REFERENCES AND NOTES

1. R. L. Siegel, K. D. Miller, N. S. Wagle, A. Jemal, Cancer statistics, 2023. *CA Cancer J. Clin.* **73**, 17–48 (2023).
2. M. Manrai, T. V. S. V. G. K. Tilak, S. Dawra, S. Srivastava, A. Singh, Current and emerging therapeutic strategies in pancreatic cancer: Challenges and opportunities. *World J. Gastroenterol.* **27**, 6572–6589 (2021).
3. V. Heinemann, S. Boeck, Perioperative management of pancreatic cancer. *Ann. Oncol.* **19** (Suppl. 7), vii273–vii278 (2008).
4. American Cancer Society, *Facts & Figures 2024* (2024); https://cancer.org/research/cancer-facts-statistics/all-cancer-facts-figures/2024-cancer-facts-figures.html.
5. D. P. S. Sohal, E. B. Kennedy, P. Cinar, T. Conroy, M. S. Copur, C. H. Crane, I. Garrido-Laguna, M. W. Lau, T. Johnson, S. Krishnamurthi, C. Moravek, E. M. O'Reilly, P. A. Philip, S. Pant, M. A. Shah, V. Sahai, H. E. Uronis, N. Zaidi, D. Laheru, Metastatic pancreatic cancer: ASCO guideline update. *J. Clin. Oncol.* **38**, 3217–3230 (2020).
6. C. Neuzillet, A. Tijeras-Raballand, P. Bourget, J. Cros, A. Couvelard, A. Sauvanet, M.-P. Vullierme, C. Tournigand, P. Hammel, State of the art and future directions of pancreatic ductal adenocarcinoma therapy. *Pharmacol. Ther.* **155**, 80–104 (2015).
7. E. Espinet, L. Klein, E. Puré, S. K. Singh, Mechanisms of PDAC subtype heterogeneity and therapy response. *Trends in cancer* **8**, 1060–1071 (2022).
8. A. A. Connor, R. E. Denroche, G. H. Jang, M. Lemire, A. Zhang, M. Chan-Seng-Yue, G. Wilson, R. C. Grant, D. Merico, I. Lungu, J. M. S. Bartlett, D. Chadwick, S.-B. Liang, J. Eagles, F. Mbabaali, J. K. Miller, P. Krzyzanowski, H. Armstrong, X. Luo, L. G. T. Jorgensen, J. M. Romero, P. Bavi, S. E. Fischer, S. Serra, S. Hafezi-Bakhtiari, D. Caglar, M. H. A. Roehrl, S. Cleary, M. A. Hollingsworth, G. M. Petersen, S. Thayer, C. H. L. Law, S. Nanji, T. Golan, A. L. Smith, A. Borgida, A. Dodd, D. Hedley, B. G. Wouters, G. M. O'Kane, J. M. Wilson, G. Zogopoulos, F. Notta, J. J. Knox, S. Gallinger, Integration of genomic and transcriptional features in pancreatic cancer reveals increased cell cycle progression in metastases. *Cancer Cell* **35**, 267–282.e7 (2019).
9. P. Bailey, D. K. Chang, K. Nones, A. L. Johns, A.-M. Patch, M.-C. Gingras, D. K. Miller, A. N. Christ, T. J. C. Bruxner, M. C. Quinn, C. Nourse, L. C. Murtaugh, I. Harliwong, S. Idrisoglu, S. Manning, E. Nourbakhsh, S. Wani, L. Fink, O. Holmes, V. Chin, M. J. Anderson, S. Kazakoff, C. Leonard, F. Newell, N. Waddell, S. Wood, Q. Xu, P. J. Wilson, N. Cloonan, K. S. Kassahn, D. Taylor, K. Quek, A. Robertson, L. Pantano, L. Mincarelli, L. N. Sanchez, L. Evers, J. Wu, M. Pinese, M. J. Cowley, M. D. Jones, E. K. Colvin, A. M. Nagrial, E. S. Humphrey, L. A. Chantrill, A. Mawson, J. Humphris, A. Chou, M. Pajic, C. J. Scarlett, A. V. Pinho, M. Giry-Laterriere, I. Rooman, J. S. Samra, J. G. Kench, J. A. Lovell, N. D. Merrett, C. W. Toon, K. Epari, N. Q. Nguyen, A. Barbour, N. Zeps, K. Moran-Jones, N. B. Jamieson, J. S. Graham, F. Duthie, K. Oien, J. Hair, R. Grützmann, A. Maitra, C. A. Iacobuzio-Donahue, C. L. Wolfgang, R. A. Morgan, R. T. Lawlor, V. Corbo, C. Bassi, B. Rusev, P. Capelli, R. Salvia, G. Tortora, D. Mukhopadhyay, G. M. Petersen, D. M. Munzy, W. E. Fisher, S. A. Karim, J. R. Eshleman, R. H. Hruban, C. Pilarsky, J. P. Morton, O. J. Sansom, A. Scarpa, E. A. Musgrove, U.-M. H. Bailey, O. Hofmann, R. L. Sutherland, D. A. Wheeler, A. J. Gill, R. A. Gibbs, J. V. Pearson, N. Waddell, A. V. Biankin, S. M. Grimmond, Genomic analyses identify molecular subtypes of pancreatic cancer. *Nature* **531**, 47–52 (2016).
10. F. Puleo, R. Nicolle, Y. Blum, J. Cros, L. Marisa, P. Demetter, E. Quertinmont, M. Svrcek, N. Elarouci, J. Iovanna, D. Franchimont, L. Verset, M. G. Galdon, J. Devière, A. de Reyniès, P. Laurent-Puig, J.-L. van Laethem, J.-B. Bachet, R. Maréchal, Stratification of pancreatic ductal adenocarcinomas based on tumor and microenvironment features. *Gastroenterology* **155**, 1999–2013.e3 (2018).
11. K. L. Aung, S. E. Fischer, R. E. Denroche, G.-H. Jang, A. Dodd, S. Creighton, B. Southwood, S.-B. Liang, D. Chadwick, A. Zhang, G. M. O'Kane, H. Albaba, S. Moura, R. C. Grant, J. K. Miller, F. Mbabaali, D. Pasternack, I. M. Lungu, J. M. S. Bartlett, S. Ghai, M. Lemire, S. Holter, A. A. Connor, R. A. Moffitt, J. J. Yeh, L. Timms, P. M. Krzyzanowski, N. Dhani, D. Hedley, F. Notta, J. M. Wilson, M. J. Moore, S. Gallinger, J. J. Knox, Genomics-driven precision medicine for advanced pancreatic cancer: Early results from the COMPASS trial. *Clin. Cancer Res.* **24**, 1344–1354 (2018).
12. M. Chan-Seng-Yue, J. C. Kim, G. W. Wilson, K. Ng, E. F. Figueroa, G. M. O'Kane, A. A. Connor, R. E. Denroche, R. C. Grant, J. McLeod, J. M. Wilson, G. H. Jang, A. Zhang, A. Dodd, S.-B. Liang, A. Borgida, D. Chadwick, S. Kalimuthu, I. Lungu, J. M. S. Bartlett, P. M. Krzyzanowski, V. Sandhu, H. Tiriac, F. E. M. Froeling, J. M. Karasinska, J. T. Topham, D. J. Renouf, D. F. Schaeffer, S. J. M. Jones, M. A. Marra, J. Laskin, R. Chetty, L. D. Stein, G. Zogopoulos, B. Haibe-Kains, P. J. Campbell, D. A. Tuveson, J. J. Knox, S. E. Fischer, S. Gallinger, F. Notta, Transcription phenotypes of pancreatic cancer are driven by genomic events during tumor evolution. *Nat. Genet.* **52**, 231–240 (2020).
13. X. Huang, G. Zhang, T. Liang, Subtyping for pancreatic cancer precision therapy. *Trends Pharmacol. Sci.* **43**, 482–494 (2022).
14. K. Miyabayashi, L. A. Baker, A. Deschênes, B. Traub, G. Caligiuri, D. Plenker, B. Alagesan, P. Belleau, S. Li, J. Kendall, G. H. Jang, R. K. Kawaguchi, T. D. D. Somerville, H. Tiriac, C.-I. Hwang, R. A. Burkhart, N. J. Roberts, L. D. Wood, R. H. Hruban, J. Gillis, A. Krasnitz, C. R. Vakoc, M. Wigler, F. Notta, S. Gallinger, Y. Park, D. A. Tuveson, Intraductal transplantation models of human pancreatic ductal adenocarcinoma reveal progressive transition of molecular subtypes. *Cancer Discov.* **10**, 1566–1589 (2020).
15. M. P. Kim, G. Lozano, Mutant p53 partners in crime. *Cell Death Differ.* **25**, 161–168 (2018).
16. F. Mantovani, L. Collavin, G. Del Sal, Mutant p53 as a guardian of the cancer cell. *Cell Death Differ.* **26**, 199–212 (2019).
17. M. Pan, C. Jiang, Z. Zhang, N. Achacoso, S. Alexeeff, A. V. Solorzano, P. Tse, E. Chung, T. Sundaresan, J. M. Suga, S. Thomas, L. A. Habel, *TP53* gain-of-function and non-gain-of-function mutations are associated with differential prognosis in advanced pancreatic ductal adenocarcinoma. *JCO Precis. Oncol.* **7**, e2200570 (2023).
18. F. K. Turrell, E. M. Kerr, M. Gao, H. Thorpe, G. J. Doherty, J. Cridge, D. Shorthouse, A. Speed, S. Samarajiwa, B. A. Hall, M. Griffiths, C. P. Martins, Lung tumors with distinct p53 mutations respond similarly to p53 targeted therapy but exhibit genotype-specific statin sensitivity. *Genes Dev.* **31**, 1339–1353 (2017).

19. R. Schulz-Heddergott, N. Stark, S. J. Edmunds, J. Li, L.-C. Conradi, H. Bohnenberger, F. Ceteci, F. R. Greten, M. Dobbelstein, U. M. Moll, Therapeutic ablation of gain-of-function mutant p53 in colorectal cancer inhibits stat3-mediated tumor growth and invasion. *Cancer Cell* **34**, 298–314.e7 (2018).
20. O. Hassin, N. B. Nataraj, M. Shreberk-Shaked, Y. Aylon, R. Yaeger, G. Fontemaggi, S. Mukherjee, M. Maddalena, A. Avioz, O. Iancu, G. Mallel, A. Gershoni, I. Grosheva, E. Feldmesser, S. Ben-Dor, O. Golani, A. Hendel, G. Blandino, D. Kelsen, Y. Yarden, M. Oren, Different hotspot p53 mutants exert distinct phenotypes and predict outcome of colorectal cancer patients. *Nat. Commun.* **13**, 2800 (2022).
21. M. P. Kim, X. Li, J. Deng, Y. Zhang, B. Dai, K. L. Allton, T. G. Hughes, C. Siangco, J. J. Augustine, Y. Kang, J. M. McDaniel, S. Xiong, E. J. Koay, F. McAllister, C. A. Bristow, T. P. Heffernan, A. Maitra, B. Liu, M. C. Barton, A. R. Wasylishen, J. B. Fleming, G. Lozano, Oncogenic *KRAS* recruits an expansive transcriptional network through mutant p53 to drive pancreatic cancer metastasis. *Cancer Discov.* **11**, 2094–2111 (2021).
22. L. Klemke, C. F. Fehlau, N. Winkler, F. Toboll, S. K. Singh, U. M. Moll, R. Schulz-Heddergott, The gain-of-function p53 R248W mutant promotes migration by STAT3 deregulation in human pancreatic cancer cells. *Front. Oncol.* **11**, 642603 (2021).
23. E. Cerami, J. Gao, U. Dogrusoz, B. E. Gross, S. O. Sumer, B. A. Aksoy, A. Jacobsen, C. J. Byrne, M. L. Heuer, E. Larsson, Y. Antipin, B. Reva, A. P. Goldberg, C. Sander, N. Schultz, The cBio cancer genomics portal: An open platform for exploring multidimensional cancer genomics data. *Cancer Discov.* **2**, 401–404 (2012).
24. S. R. Hingorani, L. Wang, A. S. Multani, C. Combs, T. B. Deramaudt, R. H. Hruban, A. K. Rustgi, S. Chang, D. A. Tuveson, *Trp53*^{R172H} and *Kras*^{G12D} cooperate to promote chromosomal instability and widely metastatic pancreatic ductal adenocarcinoma in mice. *Cancer Cell* **7**, 469–483 (2005).
25. S. Weissmueller, E. Manchado, M. Saborowski, J. P. Morris, E. Wagenblast, C. A. Davis, S.-H. Moon, N. T. Pfister, D. F. Tschaharganeh, T. Kitzing, D. Aust, E. K. Markert, J. Wu, S. M. Grimmond, C. Pilarsky, C. Prives, A. V. Biankin, S. W. Lowe, Mutant p53 drives pancreatic cancer metastasis through cell-autonomous PDGF receptor β signaling. *Cell* **157**, 382–394 (2014).
26. J. P. Morton, P. Timpson, S. A. Karim, R. A. Ridgway, D. Athineos, B. Doyle, N. B. Jamieson, K. A. Oien, A. M. Lowy, V. G. Brunton, M. C. Frame, T. R. J. Evans, O. J. Sansom, Mutant p53 drives metastasis and overcomes growth arrest/senescence in pancreatic cancer. *Proc. Natl. Acad. Sci. U.S.A.* **107**, 246–251 (2010).
27. Y.-T. Chiang, Y.-C. Chien, Y.-H. Lin, H.-H. Wu, D.-F. Lee, Y.-L. Yu, The function of the mutant p53-R175H in cancer. *Cancer* **13**, 4088 (2021).
28. The Cancer Genome Atlas Research Network, Integrated genomic characterization of pancreatic ductal adenocarcinoma. *Cancer Cell* **32**, 185–203.e13 (2017).
29. A. V. Biankin, N. Waddell, K. S. Kassahn, M.-C. Gingras, L. B. Muthuswamy, A. L. Johns, D. K. Miller, P. J. Wilson, A.-M. Patch, J. Wu, D. K. Chang, M. J. Cowley, B. B. Gardiner, S. Song, I. Harliwong, S. Idrisoglu, C. Nourse, E. Nourbakhsh, S. Manning, S. Wani, M. Gongora, M. Pajic, C. J. Scarlett, A. J. Gill, A. V. Pinho, I. Rooman, M. Anderson, O. Holmes, C. Leonard, D. Taylor, S. Wood, Q. Xu, K. Nones, J. L. Fink, A. Christ, T. Bruxner, N. Cloonan, G. Kolle, F. Newell, M. Pinese, R. S. Mead, J. L. Humphris, W. Kaplan, M. D. Jones, E. K. Colvin, A. M. Nagrial, E. S. Humphrey, A. Chou, V. T. Chin, L. A. Chantrill, A. Mawson, J. S. Samra, J. G. Kench, J. A. Lovell, R. J. Daly, N. D. Merrett, C. Toon, K. Epari, N. Q. Nguyen, A. Barbour, N. Zeps, Australian Pancreatic Cancer Genome Initiative, N. Kakkar, F. Zhao, Y. Q. Wu, M. Wang, D. M. Muzny, W. E. Fisher, F. C. Brunicardi, S. E. Hodges, J. G. Reid, J. Drummond, K. Chang, Y. Han, L. R. Lewis, H. Dinh, C. J. Buhay, T. Beck, L. Timms, M. Sam, K. Begley, A. Brown, D. Pai, A. Panchal, N. Buchner, R. De Borja, R. E. Denroche, C. K. Yung, S. Serra, N. Onetto, D. Mukhopadhyay, M.-S. Tsao, P. A. Shaw, G. M. Petersen, S. Gallinger, R. H. Hruban, A. Maitra, C. A. Iacobuzio-Donahue, R. D. Schulick, C. L. Wolfgang, R. A. Morgan, R. T. Lawlor, P. Capelli, V. Corbo, M. Scardoni, G. Tortora, M. A. Tempero, K. M. Mann, N. A. Jenkins, P. A. Perez-Mancera, D. J. Adams, D. A. Largaespada, L. F. A. Wessels, A. G. Rust, L. D. Stein, D. A. Tuveson, N. G. Copeland, E. A. Musgrove, A. Scarpa, J. R. Eshleman, T. J. Hudson, R. L. Sutherland, D. A. Wheeler, J. V. Pearson, J. D. McPherson, R. A. Gibbs, S. M. Grimmond, Pancreatic cancer genomes reveal aberrations in axon guidance pathway genes. *Nature* **491**, 399–405 (2012).
30. A. N. Bullock, J. Henckel, A. R. Fersht, Quantitative analysis of residual folding and DNA binding in mutant p53 core domain: Definition of mutant states for rescue in cancer therapy. *Oncogene* **19**, 1245–1256 (2000).
31. P. May, E. May, Twenty years of p53 research: Structural and functional aspects of the p53 protein. *Oncogene* **18**, 7621–7636 (1999).
32. A. Eldar, H. Rozenberg, Y. Diskin-Posner, R. Rohs, Z. Shakked, Structural studies of p53 inactivation by DNA-contact mutations and its rescue by suppressor mutations via alternative protein-DNA interactions. *Nucleic Acids Res.* **41**, 8748–8759 (2013).
33. M. Tu, L. Klein, E. Espinet, T. Georgomanolis, F. Wegwitz, X. Li, L. Urbach, A. Danieli-Mackay, S. Küffer, K. Bojarczuk, A. Mizi, U. Günesdogan, B. Chapuy, Z. Gu, A. Neesse, U. Kishore, P. Ströbel, E. Hessmann, S. A. Hahn, A. Trumpp, A. Papantonis, V. Ellenrieder, S. K. Singh, TNF-α-producing macrophages determine subtype identity and prognosis via AP1 enhancer reprogramming in pancreatic cancer. *Nat. Cancer* **2**, 1185–1203 (2021).
34. H.-Z. Chen, S.-Y. Tsai, G. Leone, Emerging roles of E2Fs in cancer: An exit from cell cycle control. *Nat. Rev. Cancer* **9**, 785–797 (2009).
35. J. Wang, Y. Chen, C. Huang, Q. Hao, S. X. Zeng, S. Omari, Y. Zhang, X. Zhou, H. Lu, Valosin-containing protein stabilizes mutant p53 to promote pancreatic cancer growth. *Cancer Res.* **81**, 4041–4053 (2021).
36. Y. Zhan, A. Yin, X. Su, N. Tang, Z. Zhang, Y. Chen, W. Wang, J. Wang, Interpreting the molecular mechanisms of RBBP4/7 and their roles in human diseases (Review). *Int. J. Mol. Med.* **53**, 48 (2024).
37. S. Sadasivam, J. A. DeCaprio, The DREAM complex: Master coordinator of cell cycle-dependent gene expression. *Nat. Rev. Cancer* **13**, 585–595 (2013).
38. F. A. Dick, S. M. Rubin, Molecular mechanisms underlying RB protein function. *Nat. Rev. Mol. Cell Biol.* **14**, 297–306 (2013).
39. R. Vélez-Cruz, D. G. Johnson, The retinoblastoma (RB) tumor suppressor: Pushing back against genome instability on multiple fronts. *Int. J. Mol. Sci.* **18**, 1776 (2017).
40. K. Engeland, Cell cycle regulation: p53-p21-RB signaling. *Cell Death Differ.* **29**, 946–960 (2022).
41. A. Hayashi, J. Fan, R. Chen, Y.-J. Ho, A. P. Makohon-Moore, N. Lecomte, Y. Zhong, J. Hong, J. Huang, H. Sakamoto, M. A. Attiyeh, Z. A. Kohutek, L. Zhang, A. Boumiza, R. Kappagantula, P. Baez, J. Bai, M. Lisi, K. Chadalavada, J. P. Melchor, W. Wong, G. J. Nanjangud, O. Basturk, E. M. O'Reilly, D. S. Klimstra, R. H. Hruban, L. D. Wood, M. Overholtzer, C. A. Iacobuzio-Donahue, A unifying paradigm for transcriptional heterogeneity and squamous features in pancreatic ductal adenocarcinoma. *Nat. Cancer* **1**, 59–74 (2020).
42. K. Engeland, Cell cycle arrest through indirect transcriptional repression by p53: I have a DREAM. *Cell Death Differ.* **25**, 114–132 (2018).
43. A. Chou, D. Froio, A. M. Nagrial, A. Parkin, K. J. Murphy, V. T. Chin, D. Wohl, A. Steinmann, R. Stark, A. Drury, S. N. Walters, C. Vennin, A. Burgess, M. Pinese, L. A. Chantrill, M. J. Cowley, T. J. Molloy, Australian Pancreatic Cancer Genome Initiative (APGI), N. Waddell, A. Johns, S. M. Grimmond, D. K. Chang, A. V. Biankin, O. J. Sansom, J. P. Morton, S. T. Grey, T. R. Cox, J. Turchini, J. Samra, S. J. Clarke, P. Timpson, A. J. Gill, M. Pajic, Tailored first-line and second-line CDK4-targeting treatment combinations in mouse models of pancreatic cancer. *Gut* **67**, 2142–2155 (2018).
44. C. M. Goodwin, A. M. Waters, J. E. Klomp, S. Javaid, K. L. Bryant, C. A. Stalnecker, K. Drizyte-Miller, B. Papke, R. Yang, A. M. Amparo, I. Ozkan-Dagliyan, E. Baldelli, V. Calvert, M. Pierobon, J. A. Sorrentino, A. P. Beelen, N. Bublitz, M. Lüthen, K. C. Wood, E. F. Petricoin, C. Sers, A. J. McRee, A. D. Cox, C. J. Der, Combination therapies with CDK4/6 inhibitors to treat KRAS-mutant pancreatic cancer. *Cancer Res.* **83**, 141–157 (2023).
45. J. Villanueva, Y. Yung, J. L. Walker, R. K. Assoian, ERK activity and G1 phase progression: Identifying dispensable versus essential activities and primary versus secondary targets. *Mol. Biol. Cell* **18**, 1457–1463 (2007).
46. E. S. Knudsen, V. Kumarasamy, S. Chung, A. Ruiz, P. Vail, S. Tzetzo, J. Wu, R. Nambiar, J. Sivinski, S. S. Chauhan, M. Seshadri, S. I. Abrams, J. Wang, A. K. Witkiewicz, Targeting dual signalling pathways in concert with immune checkpoints for the treatment of pancreatic cancer. *Gut* **70**, 127–138 (2021).
47. A. V. Pinho, I. Rooman, F. X. Real, p53-dependent regulation of growth, epithelial-mesenchymal transition and stemness in normal pancreatic epithelial cells. *Cell Cycle* **10**, 1312–1321 (2011).
48. K. P. Olive, D. A. Tuveson, Z. C. Ruhe, B. Yin, N. A. Willis, R. T. Bronson, D. Crowley, T. Jacks, Mutant p53 gain of function in two mouse models of Li-Fraumeni syndrome. *Cell* **119**, 847–860 (2004).
49. G. Efe, K. J. Dunbar, K. Sugiura, K. Cunningham, S. Carcamo, S. Karaiskos, Q. Tang, R. Cruz-Acuña, L. Resnick-Silverman, J. Peura, C. Lu, D. Hasson, A. J. Klein-Szanto, A. M. Taylor, J. J. Manfredi, C. Prives, A. K. Rustgi, p53 gain-of-function mutation induces metastasis via BRD4-dependent CSF-1 expression. *Cancer Discov.* **13**, 2632–2651 (2023).
50. I. H. Sahin, C. A. Iacobuzio-Donahue, E. M. O'Reilly, Molecular signature of pancreatic adenocarcinoma: An insight from genotype to phenotype and challenges for targeted therapy. *Expert Opin. Ther. Targets* **20**, 341–359 (2015).
51. H. L. Kindler, P. Hammel, M. Reni, E. van Cutsem, T. Macarulla, M. J. Hall, J. O. Park, D. Hochhauser, D. Arnold, D.-Y. Oh, A. Reinacher-Schick, G. Tortora, H. Algül, E. M. O'Reilly, S. Bordia, D. McGuinness, K. Cui, G. Y. Locker, T. Golan, Overall survival results from the POLO Trial: A phase III study of active maintenance olaparib versus placebo for germline BRCA-mutated metastatic pancreatic cancer. *J. Clin. Oncol.* **40**, 3929–3939 (2022).
52. A. Patnaik, L. S. Rosen, S. M. Tolaney, A. W. Tolcher, J. W. Goldman, L. Gandhi, K. P. Papadopoulos, M. Beeram, D. W. Rasco, J. F. Hilton, A. Nasir, R. P. Beckmann, A. E. Schade, A. D. Fulford, T. S. Nguyen, R. Martinez, P. Kulanthaivel, L. Q. Li, M. Frenzel, D. M. Cronier, E. M. Chan, K. T. Flaherty, P. Y. Wen, G. I. Shapiro, Efficacy and safety of abemaciclib, an inhibitor of CDK4 and CDK6, for patients with breast cancer, non-small cell lung cancer, and other solid tumors. *Cancer Discov.* **6**, 740–753 (2016).
53. J. Gao, B. A. Aksoy, U. Dogrusoz, G. Dresdner, B. Gross, S. O. Sumer, Y. Sun, A. Jacobsen, R. Sinha, E. Larsson, E. Cerami, C. Sander, N. Schultz, Integrative analysis of complex cancer genomics and clinical profiles using the cBioPortal. *Sci. Signal.* **6**, pl1 (2013).

54. S. Richards, N. Aziz, S. Bale, D. Bick, S. Das, J. Gastier-Foster, W. W. Grody, M. Hegde, E. Lyon, E. Spector, K. Voelkerding, H. L. Rehm, ACMG Laboratory Quality Assurance Committee, Standards and guidelines for the interpretation of sequence variants: A joint consensus recommendation of the American College of Medical Genetics and Genomics and the Association for Molecular Pathology. *Genet. Med.* **17**, 405–424 (2015).
55. S. Hänzelmann, R. Castelo, J. Guinney, GSVA: Gene set variation analysis for microarray and RNA-seq data. *BMC Bioinformatics* **14**, 7 (2013).
56. N. A. Fraunhoffer, A. M. Abuelafia, M. Bigonnet, O. Gayet, J. Roques, R. Nicolle, G. Lomberk, R. Urrutia, N. Dusetti, J. Iovanna, Multi-omics data integration and modeling unravels new mechanisms for pancreatic cancer and improves prognostic prediction. *NPJ Precision Oncol.* **6**, 57 (2022).
57. R. Nicolle, Y. Blum, L. Marisa, C. Loncle, O. Gayet, V. Moutardier, O. Turrini, M. Giovannini, B. Bian, M. Bigonnet, M. Rubis, N. Elarouci, L. Armenoult, M. Ayadi, P. Duconseil, M. Gasmi, M. Ouaissi, A. Maignan, G. Lomberk, J.-M. Boher, J. Ewald, E. Bories, J. Garnier, A. Goncalves, F. Poizat, J.-L. Raoul, V. Secq, S. Garcia, P. Grandval, M. Barraud-Blanc, E. Norguet, M. Gilabert, J.-R. Delpero, J. Roques, E. Calvo, F. Guillaumond, S. Vasseur, R. Urrutia, A. de Reyniès, N. Dusetti, J. Iovanna, Pancreatic adenocarcinoma therapeutic targets revealed by tumor-stroma cross-talk analyses in patient-derived xenografts. *Cell Rep.* **21**, 2458–2470 (2017).
58. C. J. Bruns, M. T. Harbison, H. Kuniyasu, I. Eue, I. J. Fidler, In vivo selection and characterization of metastatic variants from human pancreatic adenocarcinoma by using orthotopic implantation in nude mice. *Neoplasia* **1**, 50–62 (1999).
59. R. T. Morgan, L. K. Woods, G. E. Moore, L. A. Quinn, L. McGavran, S. G. Gordon, Human cell line (COLO 357) of metastatic pancreatic adenocarcinoma. *Int. J. Cancer* **25**, 591–598 (1980).
60. F. S. Schreiber, T. B. Deramaudt, T. B. Brunner, M. I. Boretti, K. J. Gooch, D. A. Stoffers, E. J. Bernhard, A. K. Rustgi, Successful growth and characterization of mouse pancreatic ductal cells: Functional properties of the Ki-RAS(G12V) oncogene. *Gastroenterology* **127**, 250–260 (2004).
61. I. Atanassov, H. Urlaub, Increased proteome coverage by combining PAGE and peptide isoelectric focusing: Comparative study of gel-based separation approaches. *Proteomics* **13**, 2947–2955 (2013).
62. F. Meier, A.-D. Brunner, M. Frank, A. Ha, I. Bludau, E. Voytik, S. Kaspar-Schoenefeld, M. Lubeck, O. Raether, N. Bache, R. Aebersold, B. C. Collins, H. L. Röst, M. Mann, diaPASEF: Parallel accumulation-serial fragmentation combined with data-independent acquisition. *Nat. Methods* **17**, 1229–1236 (2020).
63. S. Andrews, *FastQC: A Quality Control Tool for High-throughput Sequence Data* (Babraham Bioinformatics, 2010).
64. D. E. Wood, S. L. Salzberg, Kraken: Ultrafast metagenomic sequence classification using exact alignments. *Genome Biol.* **15**, R46 (2014).
65. S. W. Wingett, S. Andrews, FastQ Screen: A tool for multi-genome mapping and quality control. *F1000Res.* **7**, 1338 (2018).
66. A. M. Bolger, M. Lohse, B. Usadel, Trimmomatic: A flexible trimmer for Illumina sequence data. *Bioinformatics* **30**, 2114–2120 (2014).
67. A. Dobin, C. A. Davis, F. Schlesinger, J. Drenkow, C. Zaleski, S. Jha, P. Batut, M. Chaisson, T. R. Gingeras, STAR: Ultrafast universal RNA-seq aligner. *Bioinformatics* **29**, 15–21 (2013).
68. S. Anders, P. T. Pyl, W. Huber, HTSeq—A Python framework to work with high-throughput sequencing data. *Bioinformatics* **31**, 166–169 (2015).
69. P. Ewels, M. Magnusson, S. Lundin, M. Käller, MultiQC: Summarize analysis results for multiple tools and samples in a single report. *Bioinformatics* **32**, 3047–3048 (2016).
70. R. C. Gentleman, V. J. Carey, D. M. Bates, B. Bolstad, M. Dettling, S. Dudoit, B. Ellis, L. Gautier, Y. Ge, J. Gentry, K. Hornik, T. Hothorn, W. Huber, S. Iacus, R. Irizarry, F. Leisch, C. Li, M. Maechler, A. J. Rossini, G. Sawitzki, C. Smith, G. Smyth, L. Tierney, J. Y. H. Yang, J. Zhang, Bioconductor: Open software development for computational biology and bioinformatics. *Genome Biol.* **5**, R80 (2004).
71. D. Risso, J. Ngai, T. P. Speed, S. Dudoit, Normalization of RNA-seq data using factor analysis of control genes or samples. *Nat. Biotechnol.* **32**, 896–902 (2014).
72. M. I. Love, W. Huber, S. Anders, Moderated estimation of fold change and dispersion for RNA-seq data with DESeq2. *Genome Biol.* **15**, 550 (2014).
73. A. Subramanian, P. Tamayo, V. K. Mootha, S. Mukherjee, B. L. Ebert, M. A. Gillette, A. Paulovich, S. L. Pomeroy, T. R. Golub, E. S. Lander, J. P. Mesirov, Gene set enrichment analysis: A knowledge-based approach for interpreting genome-wide expression profiles. *Proc. Natl. Acad. Sci. U.S.A.* **102**, 15545–15550 (2005).
74. G. Yu, L.-G. Wang, Y. Han, Q.-Y. He, clusterProfiler: An R package for comparing biological themes among gene clusters. *OMICS* **16**, 284–287 (2012).
75. A. Liberzon, C. Birger, H. Thorvaldsdóttir, M. Ghandi, J. P. Mesirov, P. Tamayo, The Molecular Signatures Database (MSigDB) hallmark gene set collection. *Cell Syst.* **1**, 417–425 (2015).
76. B. Langmead, S. L. Salzberg, Fast gapped-read alignment with Bowtie 2. *Nat. Methods* **9**, 357–359 (2012).
77. H. Li, B. Handsaker, A. Wysoker, T. Fennell, J. Ruan, N. Homer, G. Marth, G. Abecasis, R. Durbin, 1000 Genome Project Data Processing Subgroup, The sequence alignment/map format and SAMtools. *Bioinformatics* **25**, 2078–2079 (2009).
78. A. R. Quinlan, I. M. Hall, BEDTools: A flexible suite of utilities for comparing genomic features. *Bioinformatics* **26**, 841–842 (2010).
79. Y. Zhang, T. Liu, C. A. Meyer, J. Eeckhoute, D. S. Johnson, B. E. Bernstein, C. Nusbaum, R. M. Myers, M. Brown, W. Li, X. S. Liu, Model-based analysis of ChIP-Seq (MACS). *Genome Biol.* **9**, R137 (2008).
80. L. J. Zhu, C. Gazin, N. D. Lawson, H. Pagès, S. M. Lin, D. S. Lapointe, M. R. Green, ChIPpeakAnno: A bioconductor package to annotate ChIP-seq and ChIP-chip data. *BMC Bioinformatics* **11**, 237 (2010).
81. G. Yu, L.-G. Wang, Q.-Y. He, ChIPseeker: An R/Bioconductor package for ChIP peak annotation, comparison and visualization. *Bioinformatics* **31**, 2382–2383 (2015).
82. F. Ramírez, D. P. Ryan, B. Grüning, V. Bhardwaj, F. Kilpert, A. S. Richter, S. Heyne, F. Dündar, T. Manke, deepTools2: A next generation web server for deep-sequencing data analysis. *Nucleic Acids Res.* **44**, W160–W165 (2016).
83. E. Afgan, D. Baker, B. Batut, M. van den Beek, D. Bouvier, M. Cech, J. Chilton, D. Clements, N. Coraor, B. A. Grüning, A. Guerler, J. Hillman-Jackson, S. Hiltemann, V. Jalili, H. Rasche, N. Soranzo, J. Goecks, J. Taylor, A. Nekrutenko, D. Blankenberg, The Galaxy platform for accessible, reproducible and collaborative biomedical analyses: 2018 update. *Nucleic Acids Res.* **46**, W537–W544 (2018).
84. R. C. McLeay, T. L. Bailey, Motif Enrichment Analysis: A unified framework and an evaluation on ChIP data. *BMC Bioinformatics* **11**, 165 (2010).
85. E. A. Collisson, A. Sadanandam, P. Olson, W. J. Gibb, M. Truitt, S. Gu, J. Cooc, J. Weinkle, G. E. Kim, L. Jakkula, H. S. Feiler, A. H. Ko, A. B. Olshen, K. L. Danenberg, M. A. Tempero, P. T. Spellman, D. Hanahan, J. W. Gray, Subtypes of pancreatic ductal adenocarcinoma and their differing responses to therapy. *Nat. Med.* **17**, 500–503 (2011).
86. R. A. Moffitt, R. Marayati, E. L. Flate, K. E. Volmar, S. G. H. Loeza, K. A. Hoadley, N. U. Rashid, L. A. Williams, S. C. Eaton, A. H. Chung, J. K. Smyla, J. M. Anderson, H. J. Kim, D. J. Bentrem, M. S. Talamonti, C. A. Iacobuzio-Donahue, M. A. Hollingsworth, J. J. Yeh, Virtual microdissection identifies distinct tumor- and stroma-specific subtypes of pancreatic ductal adenocarcinoma. *Nat. Genet.* **47**, 1168–1178 (2015).

Acknowledgments: We thank A. Papantonis and U. Kishore for critical reading of the manuscript. We would like to extend our thanks to K. Conrads, W. Kopp, S. Mercan, K. Reutlinger, X. Wu, and N. Sahin for technical support and assistance. We are also grateful to all the CP2 members of the KFO5002 research team for analysis of the UMG patient cohort. In addition, we express our gratitude to the Sartorius Corporate Research Department for support of this research. **Funding:** This study was supported by the Deutsche Krebshilfe through the Max-Eder (70112999 and 70115054) and Mildred-Scheel (70116314) programs, as well as the Fritz-Thyssen Stiftung (10.20.2.038MN and 10.23.2.021MN) and Wilhelm-Sander-Stiftung (2021.159.1 and 2021.159.2) to S.K.S. In addition, this study received funding from DFG for our Clinical Research Unit (KFO5002) grant to R.S.-H., E.H., V.E., and S.K.S. R.S.-H. is further funded by the Heisenberg Program of the DFG (SCHU-3160/6-1). **Author contributions:** Conceptualization: S.K.S., L.U., and LW. Methodology: S.K.S., L.U., L.W., R.S.-H., E.H., R.D.S., F.P., C.L., U.S., M.G., and N.D. Investigation: S.K.S., L.U., L.W., F.P., S.K., R.D.S., R.S.-H., E.H., L.K., U.S., V.E., C.L., N.D., and M.G. Formal analysis: S.K.S., L.U., L.W., F.P., R.D.S., E.H., L.K., C.L., and N.D. Validation: S.K.S., L.U., L.W., F.P., R.D.S., R.S.-H., L.K., V.E., U.S., and N.D. Data curation: S.K.S., L.U., L.W., C.L., and N.D. Visualization: S.K.S., L.U., L.W., and N.D. Supervision: S.K.S. Writing—original draft: S.K.S. and L.U. Writing—review and editing: S.K.S., L.U., and L.W. Project administration: S.K.S., L.U., and L.W. Resources: S.K.S., L.U., N.D., R.S.-H., E.H., U.S., C.L., M.G., and V.E. Funding: E.H., R.S.-H., V.E., and S.K.S. **Competing interests:** The authors declare that they have no competing interests. **Data and materials availability:** All data needed to evaluate the conclusions in the paper are present in the paper and/or the Supplementary Materials. The ChIP- and RNA-seq raw data generated in this study have been deposited at GEO under the accession code GSE291036.

Submitted 29 October 2024
Accepted 13 May 2025
Published 4 July 2025
10.1126/sciadv.adu2339